LA-10673-PR
Progress Report

Los Alamos National Laboratory is operated by the University of California for the United States Department of Energy under contract W-7405-ENG-36.

Space Nuclear Safety Program

October–December 1984

Los Alamos
Los Alamos National Laboratory
Los Alamos, New Mexico 87545

DISCLAIMER

The four most recent reports in this series, unclassified, are LA-10557-PR, LA-10563-PR, LA-10571-PR, and LA-10630-PR.

This work was supported by the US Department of Energy, Office of Special Nuclear Projects.

Edited by Nathana Haines
Photocomposition by Barbara Velarde Maes

Manuscript prepared by Helen Bustos, Group MST-5

LA-10673-PR
Progress Report

UC-33A
Issued: May 1986

Space Nuclear Safety Program

October–December 1984

Compiled by
T. G. George

Los Alamos Los Alamos National Laboratory
Los Alamos, New Mexico 87545

SPACE NUCLEAR SAFETY PROGRAM

October — December 1984

Compiled by

T. G. George

ABSTRACT

This quarterly report covers studies related to the use of $^{238}PuO_2$ in radioisotope power systems carried out for the Office of Special Nuclear Projects of the US Department of Energy by Los Alamos National Laboratory. Most of the studies discussed are ongoing; the results and conclusions described may change as the work progresses.

I. GENERAL-PURPOSE HEAT SOURCE (GPHS)/SAFETY VERIFICATION TEST (SVT) SERIES

A. SVT-8 Postmortem Examination (T. George)

Details of the test conditions, module disassembly, and preliminary results were given in previous monthly reports. In October, we determined the magnitude of plutonium release, obtained results of microprobe analyses, and concluded the postmortem.

1. Release Data. To determine the quantity and particle size of fines released from the breached clad (FC-391), we ultrasonically cleaned, burned, and analyzed the plutonium remains of the aeroshell and graphite impact shells (GISs). The ultrasonic cleaning solution was combined with the catch tube debris and treated in a similar manner. Because clad FC-391 was not flight quality (weld NDE value of 9.8), all of the SVT-8 test components were ashed at high temperature to permit rapid analysis. The results of all analyses are presented in Table I.

The results indicate that a total of 0.0860 g of plutonium was released.

2. Microprobe Analysis of Vent Deposits. Because previous examination of the FC-436 and FC-437 capsule vents revealed glassy deposits within and adjacent to the vent center holes (Fig. 1), cross sections of both vents were submitted for microprobe analysis. The results of the analyses indicate that both vent deposits were predominantly iridium, with low concentrations of oxygen, silicon, and tungsten. A general survey of the elements sodium through americium and specific counts for carbon, nitrogen, aluminum, phosphorus, calcium, and manganese did not reveal the presence of any other elements.

B. SVT-10 Postmortem Examination (T. George)

The test conditions, module disassembly, and preliminary results were described in previous reports. In this quarter, we completed all analyses and were able to conclude the postmortem.

1. Release Data. To establish a baseline for the quantity of plutonium released by transport through the capsule vents (no clad failures occurred in SVT-10), we burned all of the SVT-10 graphitics at high temperature and analyzed the plutonium remains. The results of the analyses (Table I) indicate that 0.0026 g of plutonium were released. It should be noted, however, that the graphite components were burned and processed for analysis within contaminated glove-box trains; the processing environment undoubtedly increased the plutonium content by some factor.

Table I. Plutonium Content of SVT Test Components

Test	Component	Plutonium Content (g)	Particle Size (μm)
SVT-8	Aeroshell	0.0061	−10
	Graphite Impact Shells	0.0046	−10
	Catch Tube Debris	0.0090	+420
		0.0083	+10 to −420
		0.0580	−10
SVT-10[a]	Aeroshell	0.0000	0
	Graphite Impact Shells	0.0026	−10

[a]No failures occurred in SVT-10.

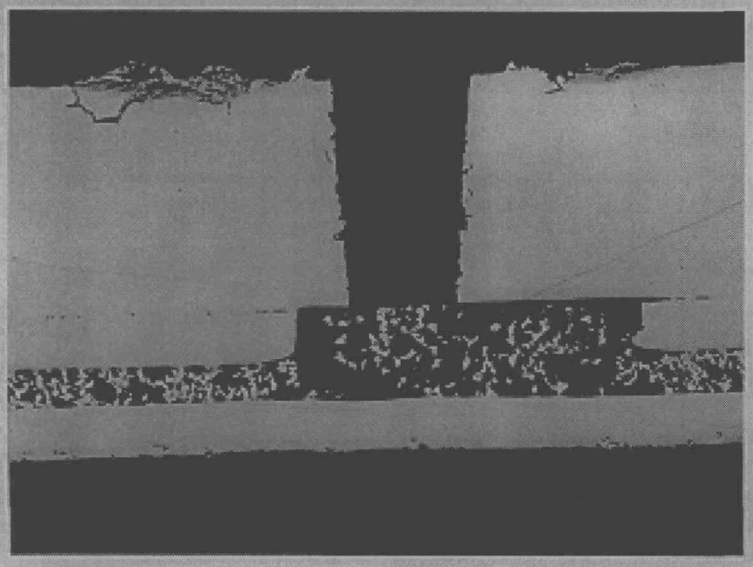

Fig. 1. Glassy deposits were observed adjacent to the FC-436 and FC-437 vent center holes. FC-436 vent, as polished, 50X.

2. Sieve Analyses. To determine the quantity of respirable fuel particles produced by the impact, we selected capsules FC-152 (secondary GIS) and FC-590 (primary GIS) for particle size analysis. Each capsule was opened and defueled underwater to prevent the loss of small fuel fragments. Results of the sieve analyses are presented in Table II.

3. Iridium Microstructures. Metallographic examination of sections from capsules FC-152, FC-589, and FC-590 revealed that the cup microstructures were generally fine grained. The FC-590 weld shield cup did however contain several coarse-grained areas (Figs. 2 and 3). The average cup grain sizes ranged from 4 to 16 grains/0.635-mm nominal wall thickness. The cup grain sizes are listed in Table III. Representative microstructures are presented in Figs. 4 through 9.

During examination of the FC-589 vent and weld shield cups, numerous delaminations were observed along the inner surfaces (Figs. 10 and 11). Although the cause of this defect is unclear, the occurrence along only the inner surfaces suggests some relation to the fuel. It is possible that the defects are not delaminations but are instead the sites of corrosion or intermetallic reactions. No similar defects were observed in any of the other capsules.

4. Weld Metallograhy. Examination of the FC-589 and FC-590 (primary clads) closure welds revealed them to be of acceptable quality. Although the FC-590 closure

Table II. SVT-10 Sieve Analyses
(All values expressed as a fraction of total pellet weight)

Particle Size	FC-152	FC-590
+ 6000	0.14470	0.25090
+2000 to 6000	0.58690	0.52880
+841 to 2000	0.18050	0.14330
+420 to 841	0.04820	0.04230
+177 to 420	0.02280	0.01990
+125 to 177	0.00370	0.00300
+74 to 125	0.00350	0.00300
+44 to 74	0.00280	0.00230
+30 to 44	0.00190	0.00160
+20 to 30	0.00250	0.00220
+10 to 20	0.00100	0.00080
+9 to 10	0.00047	0.00053
+8 to 9	0.00019	0.00027
+7 to 8	0.00027	0.00015
+6 to 7	0.00018	0.00013
+5 to 6	0.00010	0.00023
+4 to 5	0.00007	0.00009
+3 to 4	0.00006	0.00012
+2 to 3	0.00008	0.00007
+1 to 2	0.00007	0.00008
0 to 1	0.00010	0.00016
Weight Fraction <10 µm	0.00159	0.00183

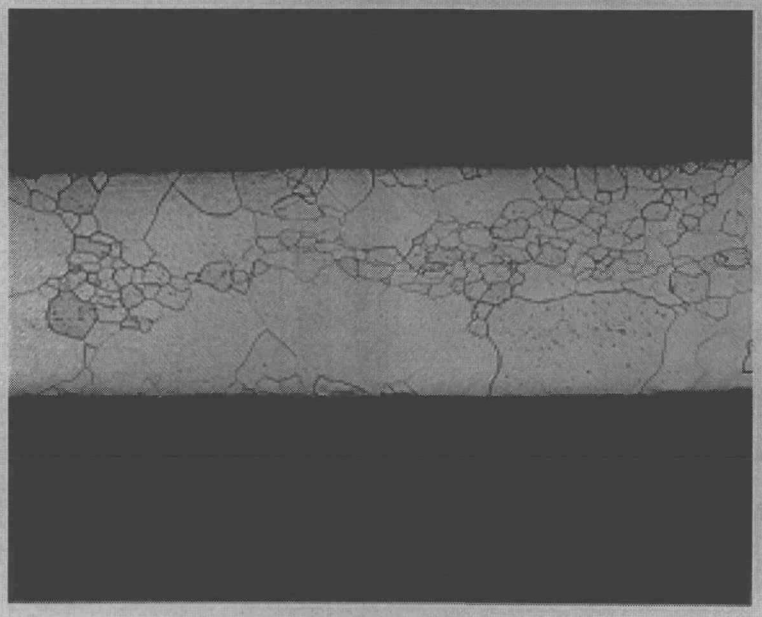

Fig. 2. An axial section of the FC-590 weld shield cup contained several abnormally large grains; 50X.

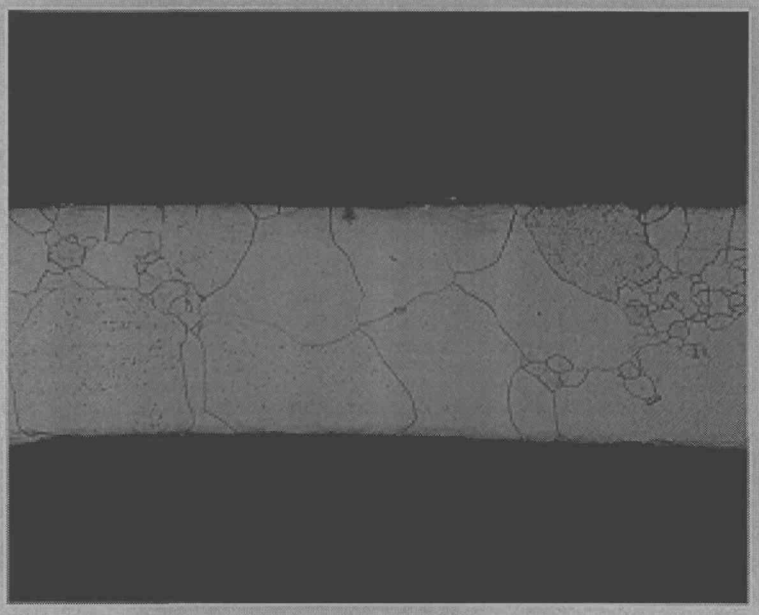

Fig. 3. Large grains were also observed in a transverse section of the FC-590 weld shield cup; 50X.

Table III. Grain Size of Selected SVT Clads

Test	Capsule	Cup	Section	Average[a] Grains/Thickness
SVT-10	FC-152	N512-5	Transverse	15.5
			Axial	ND[b]
		N516-1	Transverse	13.9
			Axial	ND
	FC-589	T115-2	Transverse	13.7
			Axial	12.0
		T113-2	Transverse	13.7
			Axial	11.0
	FC-590	V203-5	Transverse	10.7
			Axial	10.8
		V202-3	Transverse	4.2
			Axial	10.4
SVT-11	FC-345	LR324-5	Transverse	16.0
			Axial	16.0
		LR324-6	Transverse	17.0
			Axial	16.0
	FC-372	QR820-5	Transverse	17.0
			Axial	16.0
		QR820-4	Transverse	19.0
			Axial	19.0

[a]Average number of grains/0.635-mm nominal wall thickness.
[b]Not determined.

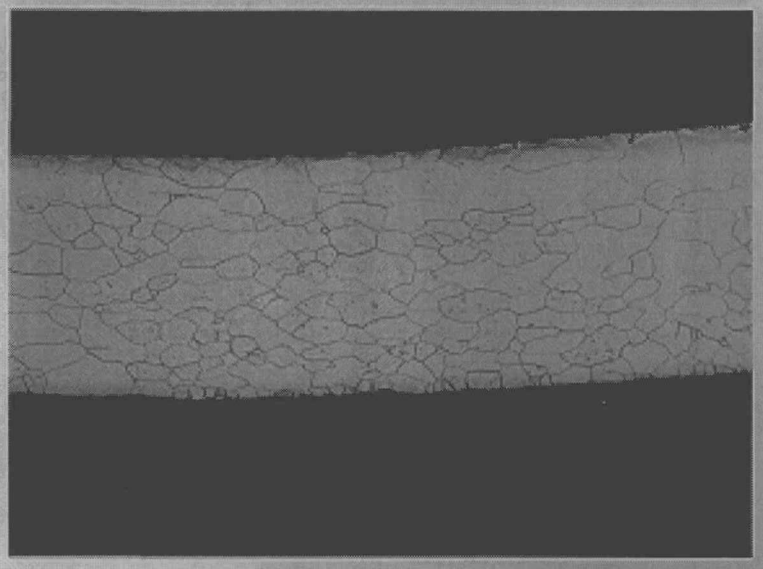

Fig. 4. The FC-589 vent cup had a fine-grained microstructure; transverse section, 50X.

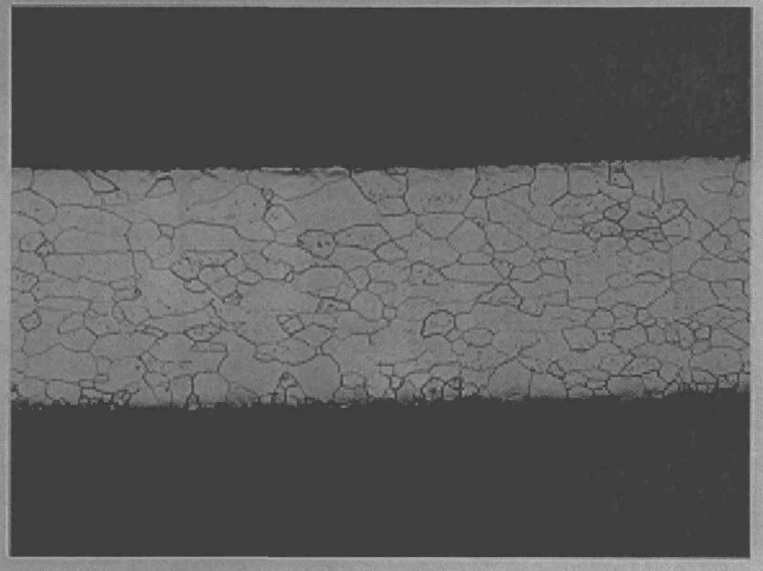

Fig. 5. The FC-589 weld shield cup had an acceptable microstructure; transverse section, 50X.

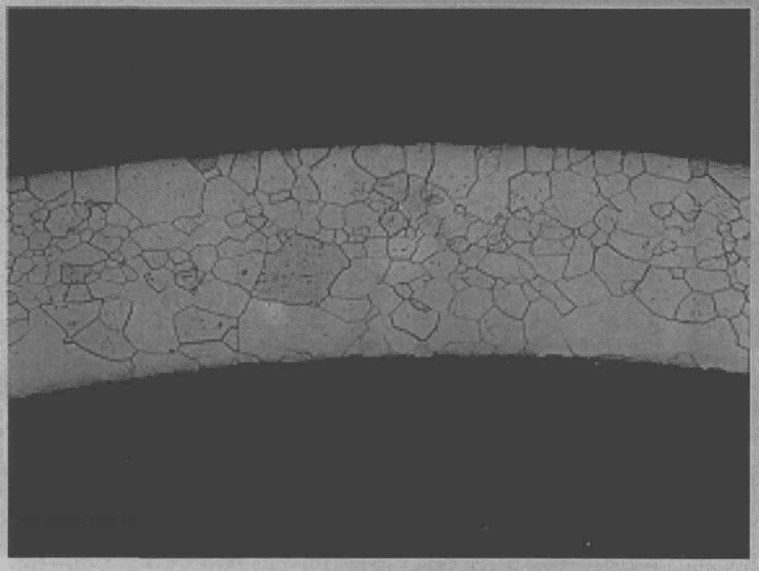

Fig. 6. The FC-590 vent cup had a generally fine grained microstructure; axial section, 50X.

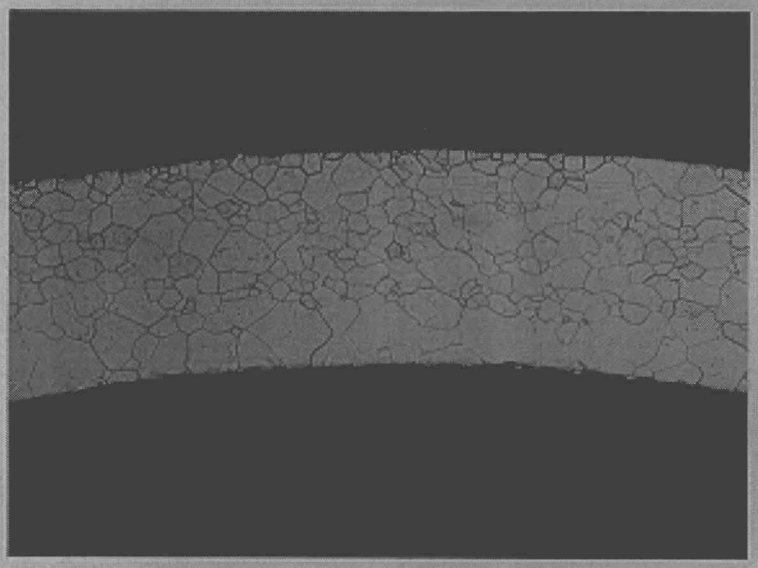

Fig. 7. Although the FC-590 weld shield cup contained some areas of excessive grain growth, the microstructure was generally acceptable; axial section, 50X.

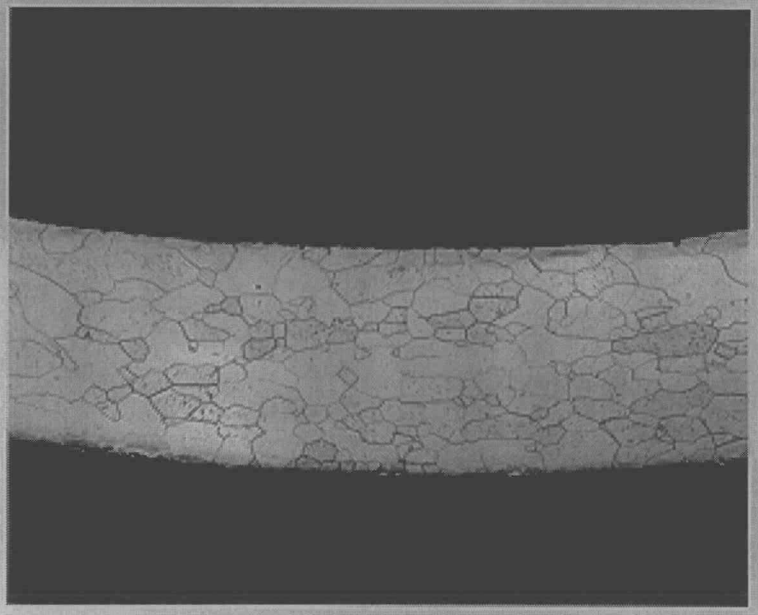

Fig. 8. The microstructure of the FC-152 vent cup was acceptable; axial section, 50X.

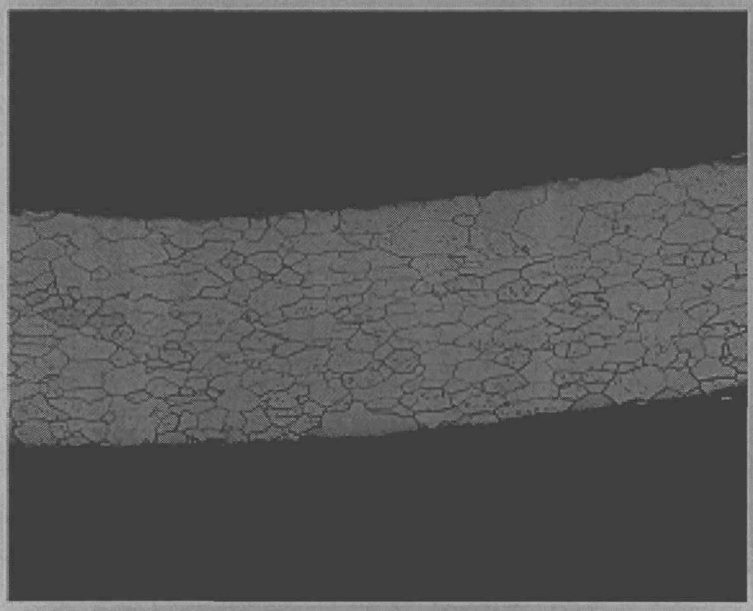

Fig. 9. The FC-152 weld shield cup had a fine-grained microstructure; transverse section, 50X.

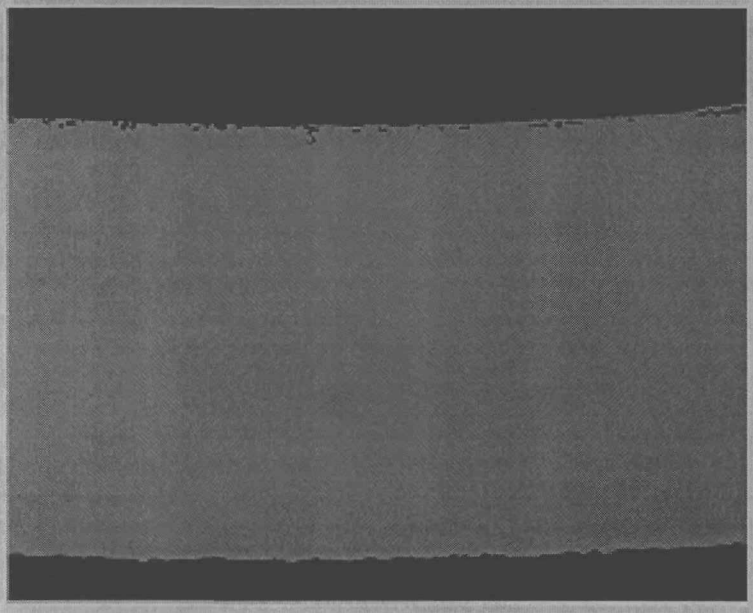

Fig. 10. Several subsurface delaminations were observed on the interior of the FC-589 vent cup; 100X.

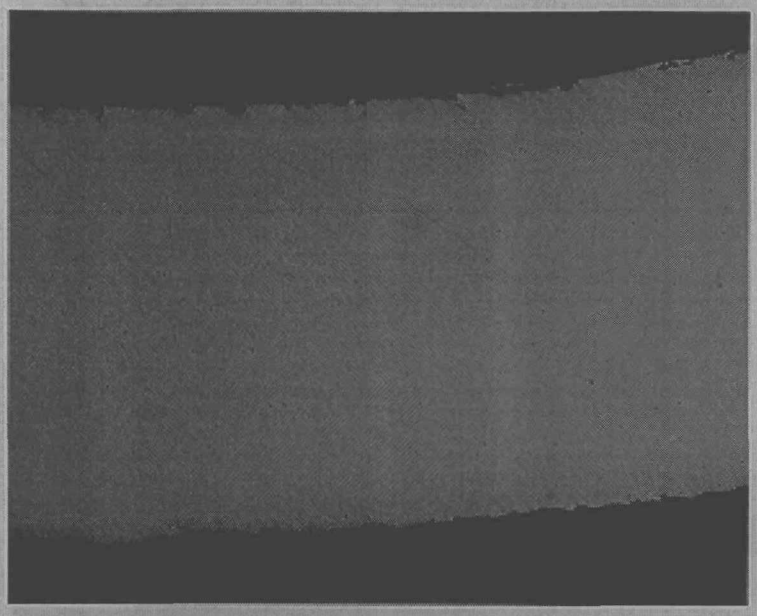

Fig. 11. Similar delaminations were observed on the interior of the FC-589 weld shield cup; 100X.

weld contained a significant amount of porosity (Fig. 12a), the microstructure (though somewhat coarse) was satisfactory (Fig. 12b). The FC-589 weld had a typical microstructure and contained no observable defects (Fig. 13).

Examination of the FC-152 closure weld revealed a slight wall misalignment (Fig. 14a) and evidence of incomplete weld penetration (Fig. 14b).

5. Vent Metallography. Microscopic examination of the FC-589 and FC-590 capsule vents revealed no mechanical defects. The vent frits were uniform and properly aligned. Because the capsules experienced only moderate deformation, neither vent was damaged by the impact. Both vents were free of intermetallic deposits.

Examination of the vent cover welds revealed evidence of abnormal grain growth (Figs. 15 and 16). Although large grains were observed near both cover welds, the FC-590 weld was worst affected; wall sections adjacent to the FC-590 weld were only 2 grains thick (Fig. 16).

6. Fuel Ceramography. We sampled each fuel pellet to provide a specimen for ceramography. Microscopic examination of the polished samples did not reveal any unusual features (Figs. 17 through 20). The fuel microstructures were typical of SRP production and were similar to the microstructures of pellets used in previous SVT impacts.

7. Analytical Results. Specimens for spectrographic analysis were removed from the FC-152, FC-589, and FC-590 iridium cups. Results of the analyses (Table IV) indicate that all of the iridium cups contained unusual amounts of iron (275-550 ppm). In addition, both of the FC-590 cups had elevated copper, aluminum, silicon, chromium, and nickel contents.

Auger electron spectroscopy (AES) analyses (Table V) of specimens removed from capsules FC-589 and FC-590 revealed significant thorium depletion on all of the cup interiors. The thorium concentration on the interior of one FC-589 shield cup section was below the detection limit of the instrument. Oddly, no abnormal grain growth was observed in an electron micrograph of this sample. Grain coarsening was, however, observed in micrographs of FC-590 shield cup section No. 2. Significant amounts of sulfur were also observed in all of the FC-590 cup sections.

Spectrographic and radiochemical analyses of the fuel pellets (Table VI) did not reveal any significant abnormalities. The calcium contents were, however, somewhat higher than usual.

C. SVT-11 Postmortem Examination (D. Pavone)

Previous SVT impacts were conducted using hardened steel targets. For comparison of the GPHS module response to impact against target materials with elastic moduli different than that of steel, the SVT-11 test

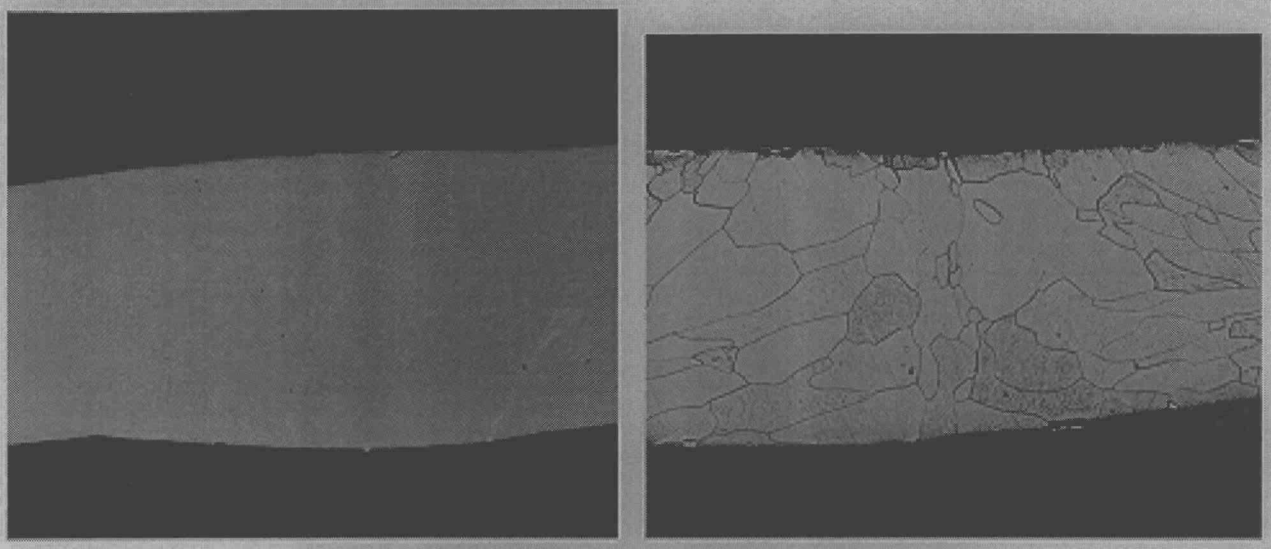

(a) (b)

Fig. 12. The FC-590 closure weld contained a significant amount of porosity and had a somewhat coarse microstructure. (a) Polished and (b) etched; both at 50X.

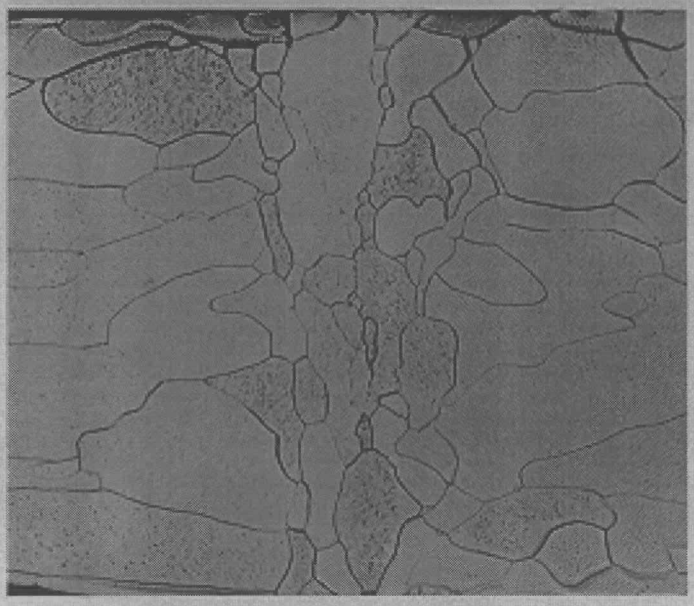

Fig. 13. The FC-589 weld had a typical microstructure; etched, 100X.

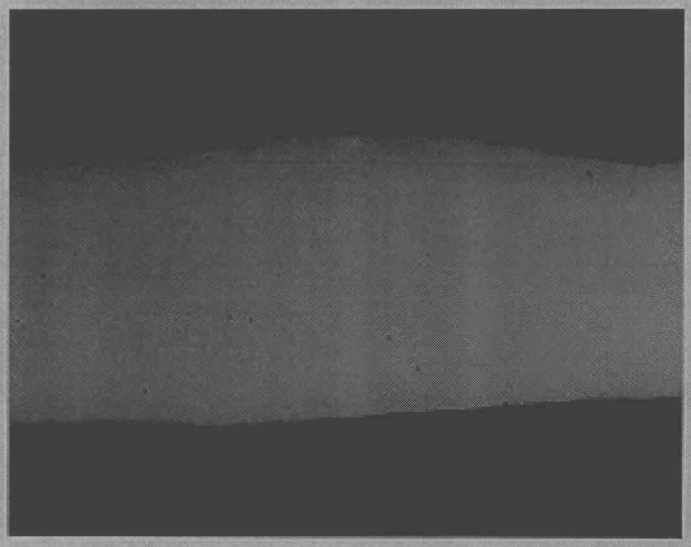

(a)

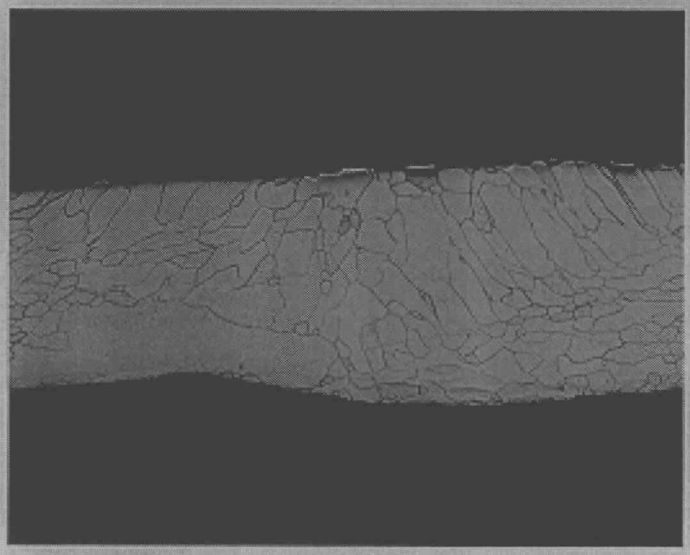

(b)

Fig. 14. The FC-152 closure weld was not of good quality. (a) Polished and (b) etched; both at 50X.

(a)

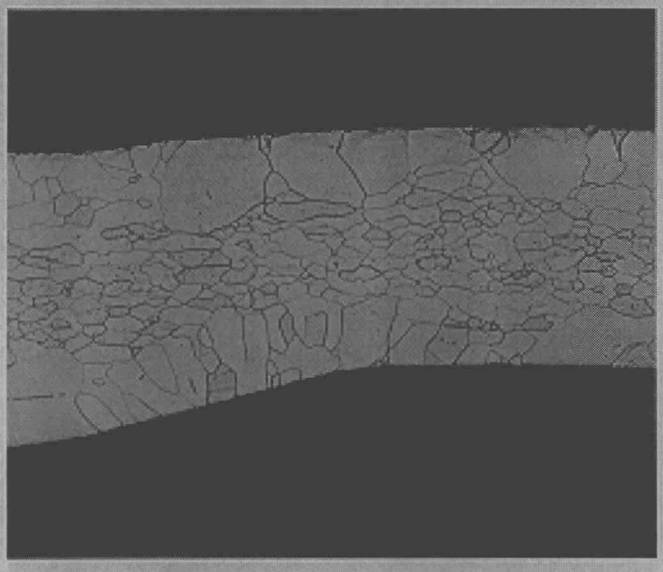

(b)

Fig. 15. Abnormal grain growth was observed on both sides of the FC-589 vent cover weld. (a) Impact face side and (b) trailing face; both at 50X.

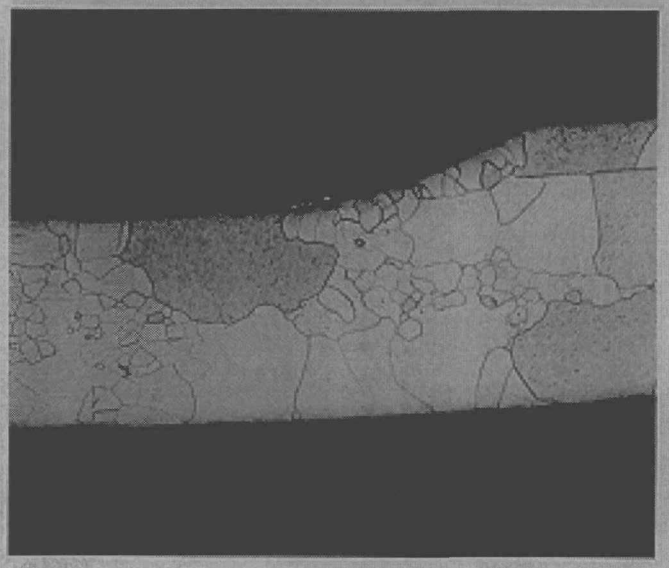

(a)

(b)

Fig. 16. The FC-590 vent cover weld was also affected by excessive grain growth. (a) Impact face side and (b) trailing face; both at 50X.

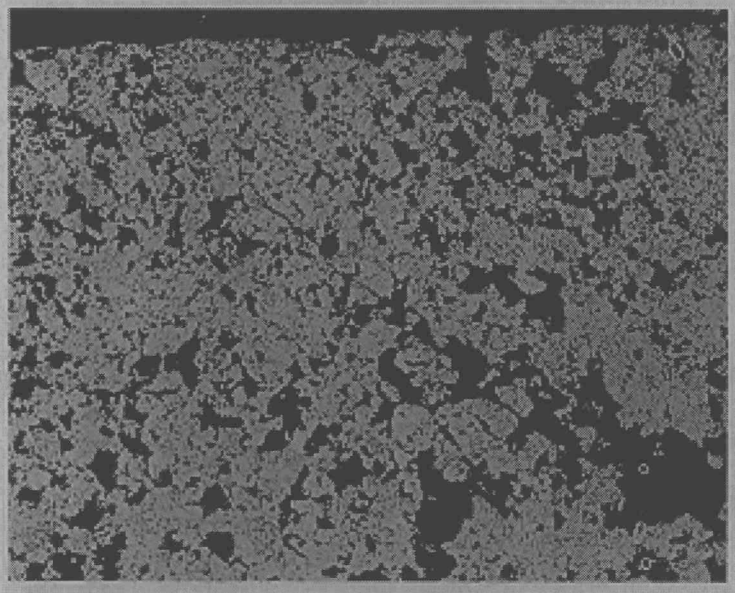

Fig. 17. The HF-152 fuel pellet had a typical microstructure; etched, 100X.

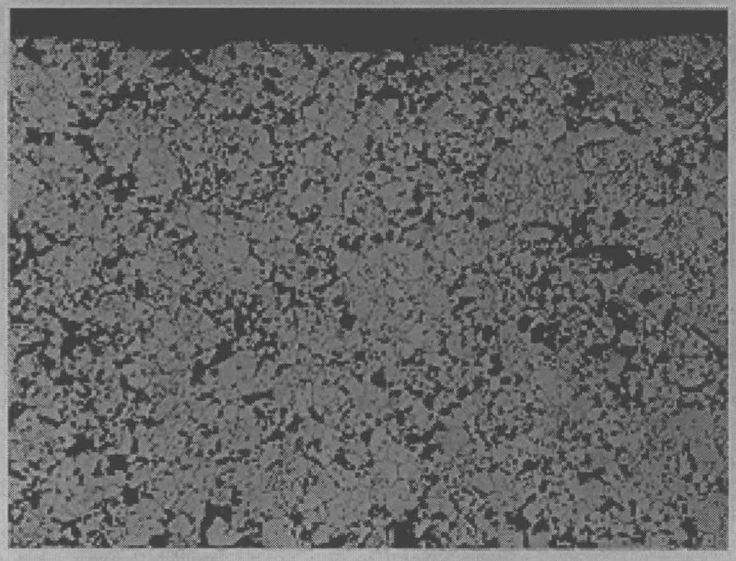

Fig. 18. No unusual features were observed in the microstructure of the HF-185 fuel pellet; etched, 100X.

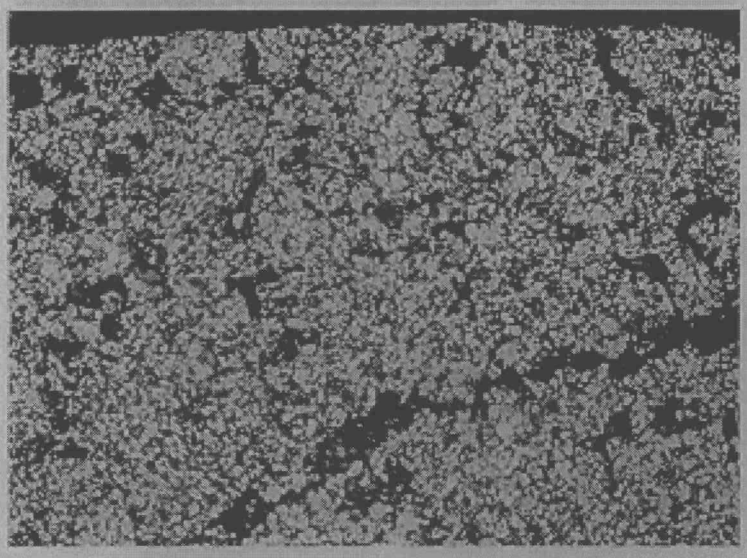

Fig. 19. The HF-589 fuel pellet had a typical microstructure; etched, 100X.

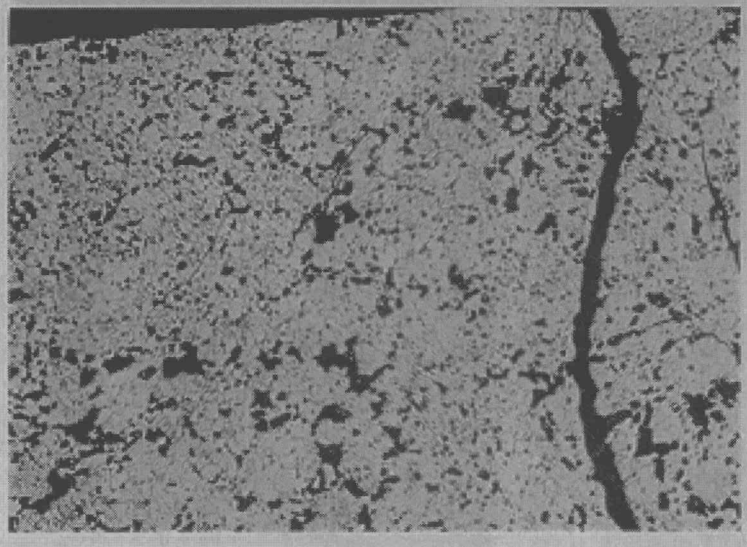

Fig. 20. No unusual features were observed in the microstructure of the HF-590 fuel pellet; etched, 100X.

Table IV. Spectrographic Analyses of Selected SVT Clads

Capsule	Cup	Elements[a] (ppm)								
		Cu	Mg	Ca	Al	Si	Cr	Fe	Ni	Pt
FC-152	N512-5	10	15	ND[b]	70	15	80	500	100	30
	N516-1	10	5	ND	100	15	60	400	80	30
FC-589	T113-2	4	ND	3	25	ND	20	275	10	ND
	T115-2	5	7	3	50	15	25	300	25	ND
FC-590	V202-3	45	20	10	225	85	200	450	200	30
	V203-5	60	20	10	200	125	200	550	225	30
FC-345	LR324-5	5	5	ND	50	ND	30	300	30	ND
	LR324-6	5	3	ND	60	ND	20	200	20	30
FC-372	QR820-5	20	3	ND	60	20	20	200	40	ND
	QR820-4	5	ND	ND	60	ND	20	200	20	ND

[a]Elements are listed only if they exceed the detectability limit in at least one specimen.
[b]None detected.

assembly was impacted against a concrete target. The test components were aged 90 days at 1287°C (clad) in vacuum and subjected to a reentry. The module orientation was $\alpha = \beta = 0°$, and the impact temperature was 975°C (clad). Impact velocity was 54.4 m/s. Graphite components of the test assembly are listed in Table VII, and encapsulation details for the SVT-11 fueled clads are given in Table VIII. Data describing the SVT-11 fuel pellets are presented in Table IX.

Continuous monitoring of helium release during the aging treatment did not indicate any evidence of vent plugging.

After the test, the impacted module (contained within a sealed catch tube) was transferred to the CMR building for disassembly. The interior of the catch tube was wet and lightly corroded by alkaline liquid driven from the concrete. Although the aeroshell closures were slightly dislodged, the module was essentially intact. Photographs of the impacted module are shown in Fig. 21. Damage to the aeroshell was substantially less than that incurred at this orientation in impacts against the steel targets. There were no fractures on the impact face, but fractures were present on the center of the nonclosure narrow faces parallel to the impact shell axes. The aeroshell back was dented and cracked in the center. Figure 22 shows an obliquely illuminated photograph of the concrete target in which the imprint of the aeroshell can be seen. There were no major fractures in the concrete target. However, reproduction of the graphite surface features in the imprint suggests that extensive microcracking did occur. Neither GIS was fractured on the impact face, but a slightly bowed profile, illustrated in Fig. 23, was observed.

No failures of the iridium capsules occurred. Photographs of the fueled clads are shown in Fig. 24; the gross deformations are tabulated in Table X. For comparison, the average deformations of 16 fueled clads (SVT-1 through SVT-4), impacted in the same orientation against steel targets, are also listed in Table X. The overall deformation of each fueled clad in this test was less than the average of those tested against steel targets.

The most severe localized iridium deformation occurred on the center of the FC-345 impact face. Figure 25 shows two fuel fragment indentations with shallow re-entrant folds. No evidence of iridium failure was detected by subsequent metallographic examination.

The iridium cup microstructures of the primary fueled clads were nonuniform across the thickness. Large grains observed on the cup interiors extended through 20-25% of the wall thicknesses. Typical cup microstructures are shown in Fig. 26, and the average number of grains/0.635-mm nominal wall thickness are tabulated in Table III. Although the grain size of cup QR820-4 (FC-372) was finer than that of the others, all of the cup microstructures were consistent with the grain sizes observed in previous test clads.

Results of AES analysis of the iridium grain boundary chemistry are tabulated in Table V. Thorium depletion at the cup interiors varied from modest in the FC-372 shield cup to severe in the other samples analyzed. Very minor quantities of phosphorus were also detected in some samples. In addition, three FC-372 samples exhibited high concentrations of sulfur; small amounts of sulfur were also detected in the fourth FC-372 sample, as well as in one FC-345 sample. The absence of clad failures suggests that these levels of sulfur can be tolerated. As usual, carbon and oxygen were present in widely varying quantities in all samples.

Table V. Iridium AES Analyses

Specimen		Th_{65}/Ir_{229} Int.	Center	Ext.	(Av)	P_{120}/Ir_{229} (Av)	C_{270}/Ir_{229} (Av)	O_{510}/Ir_{229} (Av)	S_{150}/Ir_{229} (Av)	Cl_{180}/Ir_{229} (Av)
FC-589	V-cup 1	0.05	0.44	0.38	0.29	ND[a]	0.05	0.57	ND	ND
	V-cup 2	0.04	0.62	0.51	0.39	ND	0.07	0.65	0.06	0.02
	S-cup 1	0.04	0.37	0.37	0.26	ND	0.05	0.67	0.03	0.06
	S-cup 2	ND	0.30	0.28	0.19	ND	0.04	0.18	ND	ND
FC-590	V-cup 1	0.04	0.16	0.48	0.23	ND	0.08	1.24	0.87	0.14
	V-cup 2	0.04	0.55	0.54	0.38	ND	0.07	0.96	0.82	0.05
	S-cup 1	0.03	0.40	0.20	0.21	ND	0.05	0.94	0.76	0.05
	S-cup 2	0.04	0.08	0.47	0.20	ND	0.08	0.76	0.10	0.21
FC-345	V-cup 1	0.07	0.15	0.41	0.22	ND	0.57	0.98	0.09	ND
	V-cup 2	ND	0.72	0.36	0.36	0.03	0.09	0.47	ND	0.05
	S-cup 1	0.07	0.48	0.33	0.29	0.02	0.28	0.83	ND	ND
	S-cup 2	0.20	0.57	0.57	0.45	ND	0.22	0.57	ND	ND
FC-372	V-cup 1	0.07	0.56	0.57	0.40	ND	0.67	1.10	S[b]	ND
	V-cup 2	0.20	0.48	0.39	0.36	0.02	0.95	0.98	S	0.24
	S-cup 1	0.38	0.44	0.44	0.42	ND	1.09	1.01	S	0.06
	S-cup 2	0.46	0.53	0.46	0.49	0.02	0.20	0.63	0.04	ND

[a]*None detected.*
[b]Strong indication.

Table VI. Spectrographic and Radiochemical Analyses of SVT Fuel Pellets

Pellet	Test	Selected Elements[a] (ppm)								
		P	Ni	Mg	Ca	Al	Si	Fe	Cr	Ti
HF-152	SVT-10	5	ND[b]	2	750	140	25	25	5	35
HF-185	SVT-10	6	ND	1	400	ND	8	10	15	25
HF-589	SVT-10	6	ND	1	500	ND	10	ND	7	35
HF-590	SVT-10	2	ND	10	750	30	35	15	8	20
HF-341	SVT-11	ND	ND	5	200	30	20	30	ND	15
HF-345	SVT-11	16	ND	2	50	ND	40	85	ND	50
HF-365	SVT-11	2	ND	10	100	25	30	20	ND	10
HF-372	SVT-11	2	ND	8	30	25	20	30	ND	20
HF-209	BCI-1	3	25	20	100	35	80	180	25	20
HF-164	BCI-2	2	ND	ND	50	ND	10	120	30	40
HF-351	BCI-3	3	ND	ND	50	ND	20	70	15	40

[a]Elements are listed only if they exceed the detectability limit in at least one specimen.
[b]None detected.

Table VII. SVT Graphite Components

	SVT-11	SVT-12
Aeroshell	PAL-010	PAT-1028
Prime Impact Shell	PGL-008	PGT-1071
Insulation Sleeve	C-40-3	C-56-4
Insulation Disks	P-8-2-15	P-13-2-27
	P-11-1-17	P-13-2-27
Secondary Impact Shell	PGL-012	PGT-1072
Insulation Sleeve	C-39-3	C-56-5
	P-12-1-20	P-13-2-36
Insulation Disks	P-11-1-21	P-13-2-38

Table VIII. Encapsulation Details for SVT Fueled Clads

Test	Capsule	Value	Iridium		Fuel Pellet
			Vent Cup	Shield Cup	
SVT-11	FC-341	9.3	PR725-2	PR726-3	HF-341
	FC-345	7.6	LR324-5	LR324-6	HF-345
	FC-365	8.9	PR727-1	PR727-4	HF-365
	FC-372	8.2	QR820-5	QR821-4	HF-372
SVT-12	FC-226	14.0	P703-4	P703-5	HF-226
	FC-277	12.9	MR432-3	MER16-6	HF-277
	FC-628	1.3	S-11.1	TR-121.2	HF-628
	FC-629	1.3	TR-128.1	TR-127.5	HF-629

Table IX. Data for SVT Fuel Pellets

Test	Pellet	Diameter (mm)	Length (mm)	Weight (g)	Processing Atmosphere
SVT-11	HF-341	27.8	28.1	150.6	Ar
	HF-345	27.7	27.5	150.5	Ar
	HF-365	NI[a]	NI	150.4	Ar
	HF-372	27.4	27.4	150.5	Ar
SVT-12	HF-226	27.5	NI	150.3	$Ar/0_2$
	HF-277	27.5	27.4	150.4	$Ar/0_2$
	HF-628	27.7	28.0	149.3	Ar
	HF-629	27.5	27.9	149.4	Ar

[a]Not integral at loading.

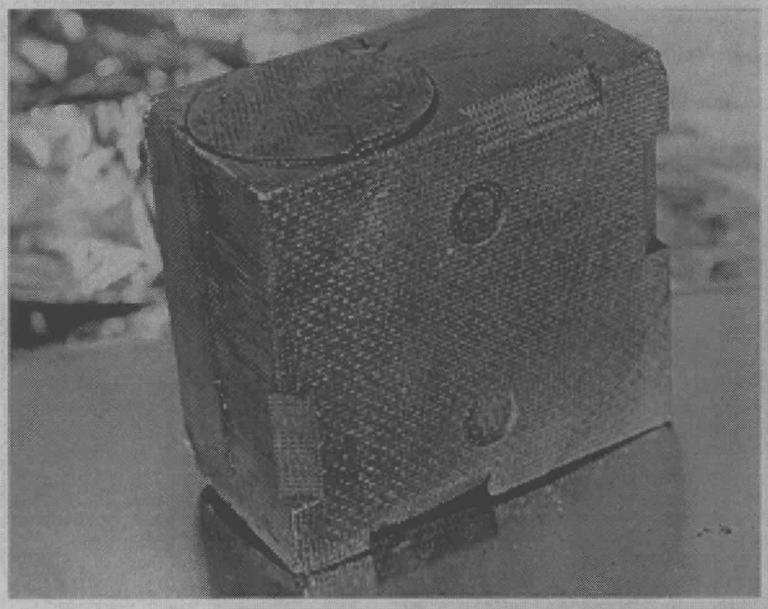

(a)

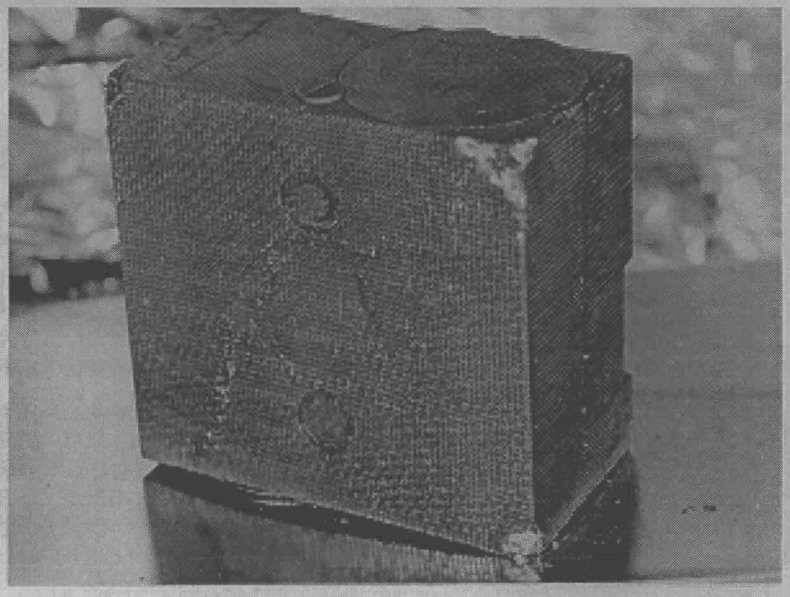

(b)

Fig. 21. Damage incurred by the aeroshell in SVT-11 was less than that in impact tests against a steel target. (a) Impact face forward and (b) back side forward.

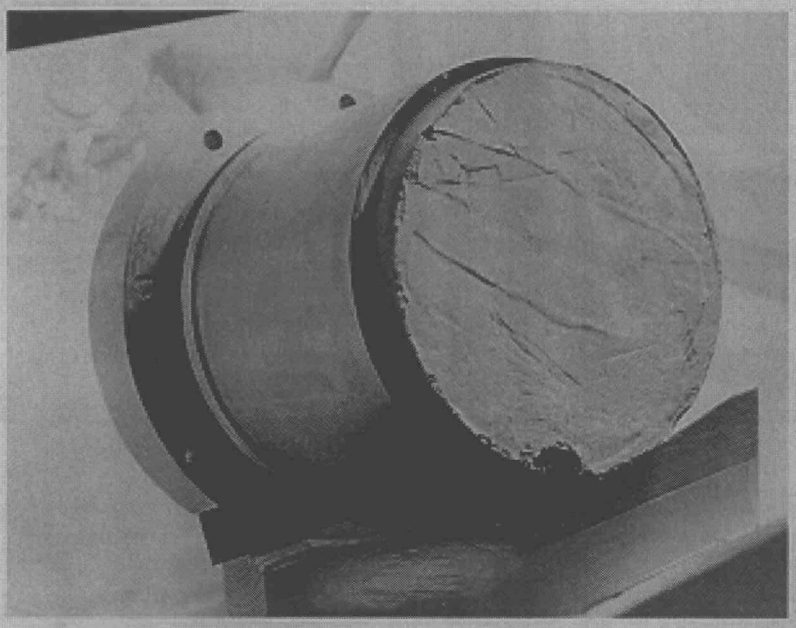

Fig. 22. An imprint of the aeroshell was present on the concrete target face in SVT-11.

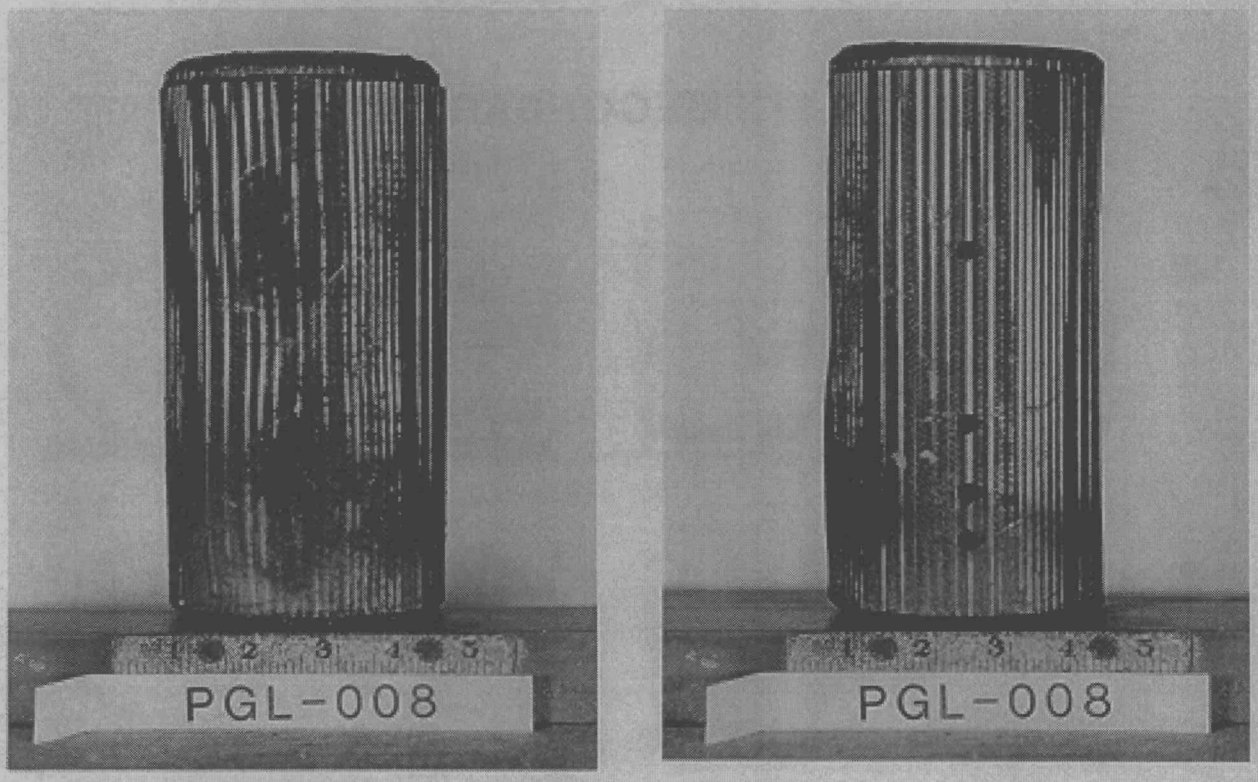

(a) (b)

Fig. 23. Axial fractures on the impact face of the GISs did not occur in SVT-11, though a typical slightly bowed profile was present. (a) Impact face and (b) profile view.

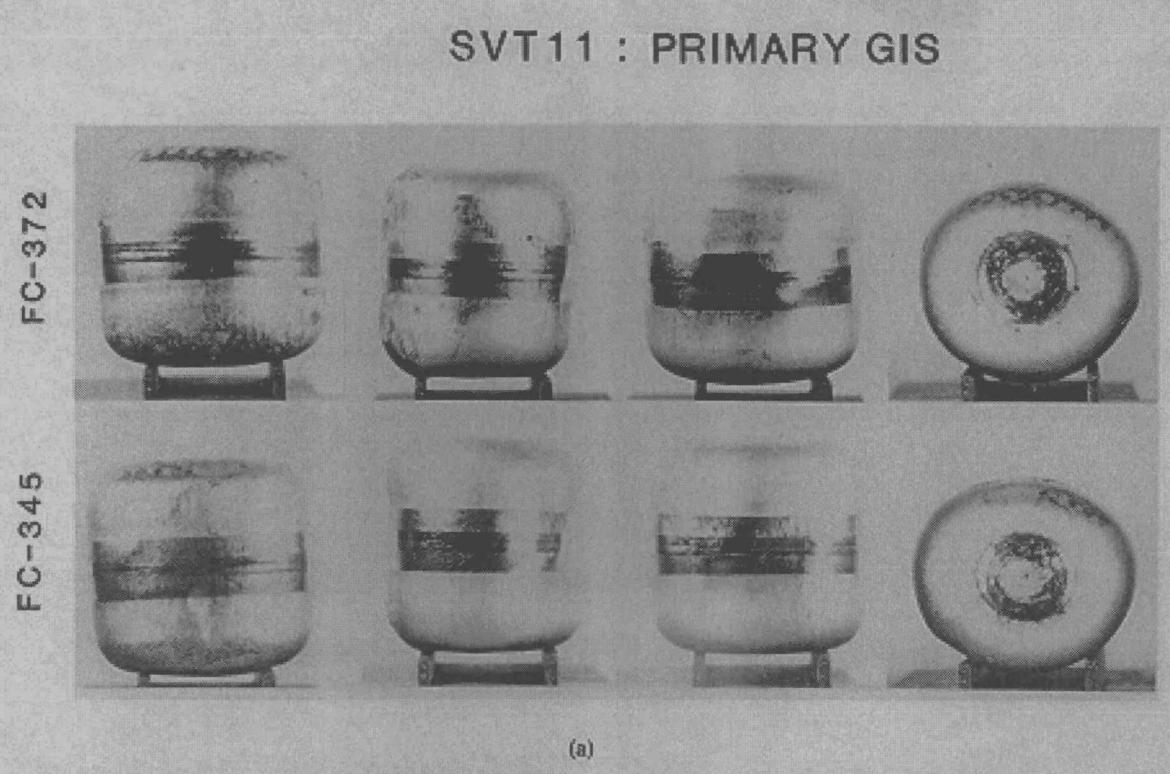

(a)

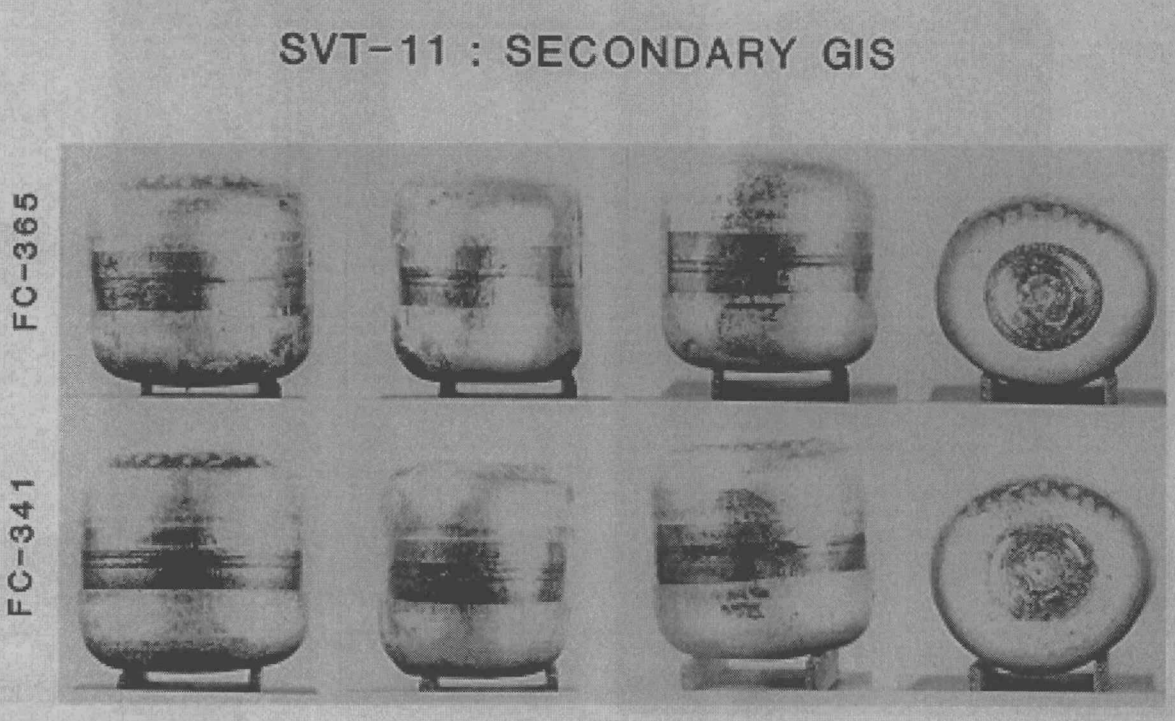

(b)

Fig. 24. No failures of the iridium clad occurred in the SVT-11 fueled clads. The overall deformation was less than that of the impacts against steel targets.

Table X. SVT Test Summaries

Test	Fueled Clads	Clad NDE Value	Gross Deformation (%) Diam	Height	Axial	Failures No.	Areas (mm^2)
SVT-11	FC-372	8.2	+ 6.8	− 7.1	+2.9	0	
	FC-345	7.6	+ 8.2	− 7.9	+3.2	0	0
	FC-365	8.9	+ 7.0	− 8.9	+1.7	0	
	FC-341	9.3	+ 9.1	− 8.2	+2.7	0	
SVT-12	FC-628	1.3	+ 8.9	− 5.1	+4.5	2	
	FC-629	1.3	+ 8.8	− 9.1	+6.1	0	17.0
	FC-226	14.0	+13.0	−11.5	+6.2	1	
	FC-277	12.9	+10.4	− 9.8	+5.6	0	

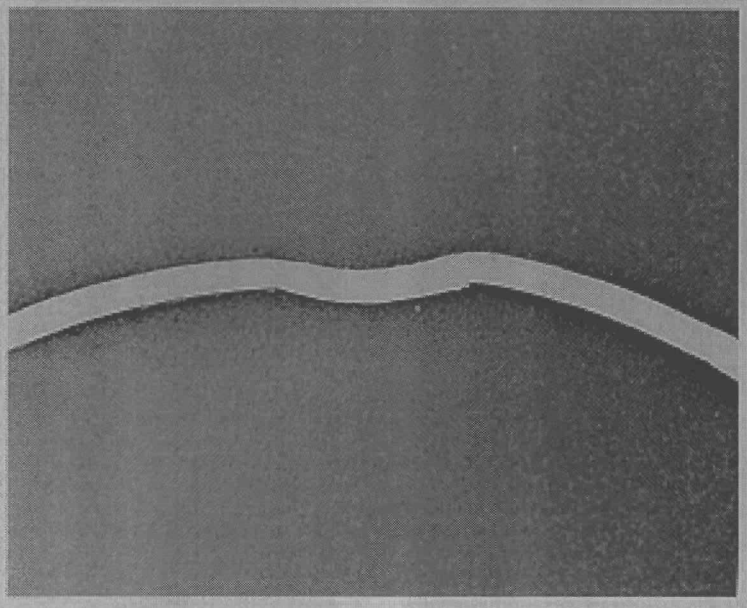

Fig. 25. No failures of the iridium were observed at the location of most severe iridium deformation in FC-345 of SVT-11; ~7X.

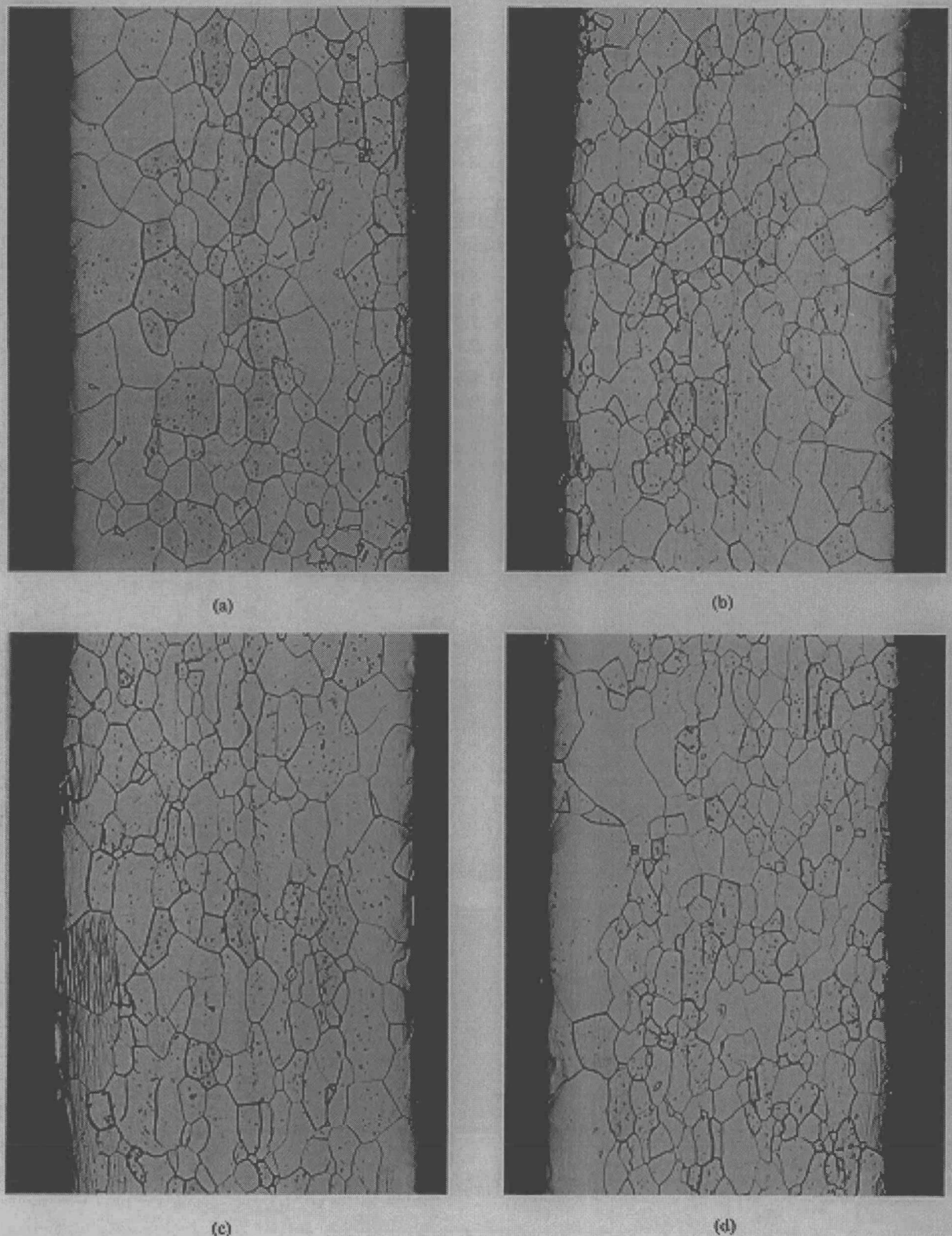

Fig. 26. Iridium microstructures in SVT-11 were nonuniform across the wall thickness. (a) FC-345 vent cup, (b) FC-345 shield cup, (c) FC-372 vent cup, and (d) FC-372 shield cup; all at 100X.

Iron was the principal impurity element detected by electron spectrographic analysis of the iridium. The quantities of iron (200-300 ppm) were comparable to those observed in other samples in this test series. The spectrographic results are tabulated in Table IV.

The welds of both primary fueled clads were free of porosity. The welds penetrated the wall thickness completely and possessed desirable microstructures.

Results of spectrographic analysis of samples of the plutonia pellets are tabulated in Table VI. The calcium contents of pellets HF-372, HF-341, and HF-365 were initially reported to be 750, >750, and 700 ppm, respectively. Repeat samples were run after carefully cleaning the spectrographic sample preparation and arc chamber facilities. Results for calcium from the repeat samples were 30, 200, and 100 ppm, respectively. It therefore appears that the original results were in error because of inadvertant sample contamination. High calcium contents (≈700 ppm) were also reported for plutonia pellets from SVT-9; these results were likely biased by the same problem.

The HF-372 and HF-345 pellet microstructures were typical of SRP fabricated fuel. No second-phase impurities were observed in either sample.

Metallographic examination of cross sections of the FC-345 and FC-372 vent assemblies indicated no vapor transported deposits in the vent orifices and only small amounts of plutonia deposited at the entrances to the vent filter elements. The decontamination cover welds and the vent assembly welds were free of cracks and porosity. However, in both fueled clads, abnormal grain growth in the parent metal on one side of the cross section was observed (Fig. 27).

D. SVT-12: Test and Postmortem (T. George)

On December 13, 1984, a fully loaded GPHS module was impacted at 75.5 m/s and 975°C. The module orientation was $\alpha = \beta = \gamma = 0°$ (Fig. 28), and the target material was concrete. Before impact, the test assembly was subjected to a simulated reentry cycle at 1375°C. In addition, the fueled clads had been aged for 90 days at 1287°C. The SVT-12 graphite components are listed in Table VII and encapsulated details for the SVT-12 fueled clads are given in Table VIII. Data describing the fuel pellets are presented in Table IX. After the test, a sealed catch tube containing the impacted module was

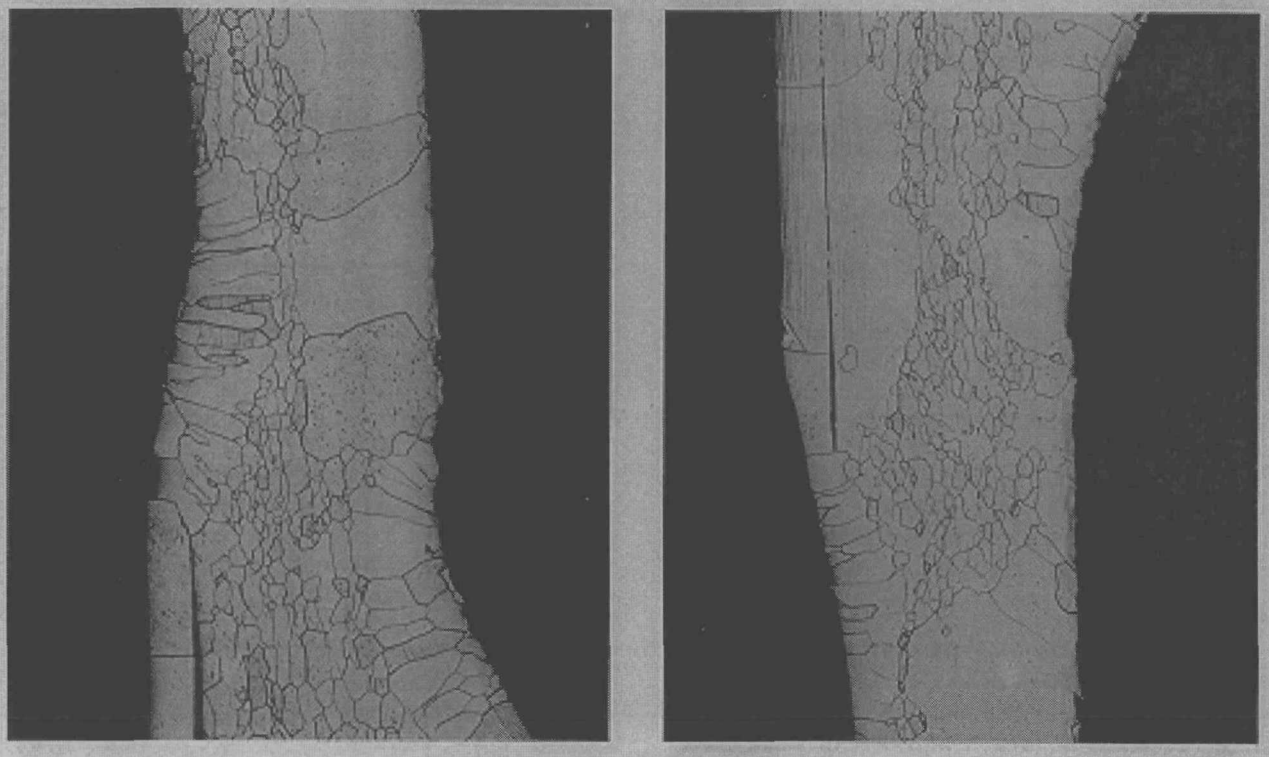

(a) (b)

Fig. 27. Abnormal grain growth occurred in the vent assembly welds of the primary fueled clads of SVT-11. (a) FC-345 and (b) FC-372; both at 50X.

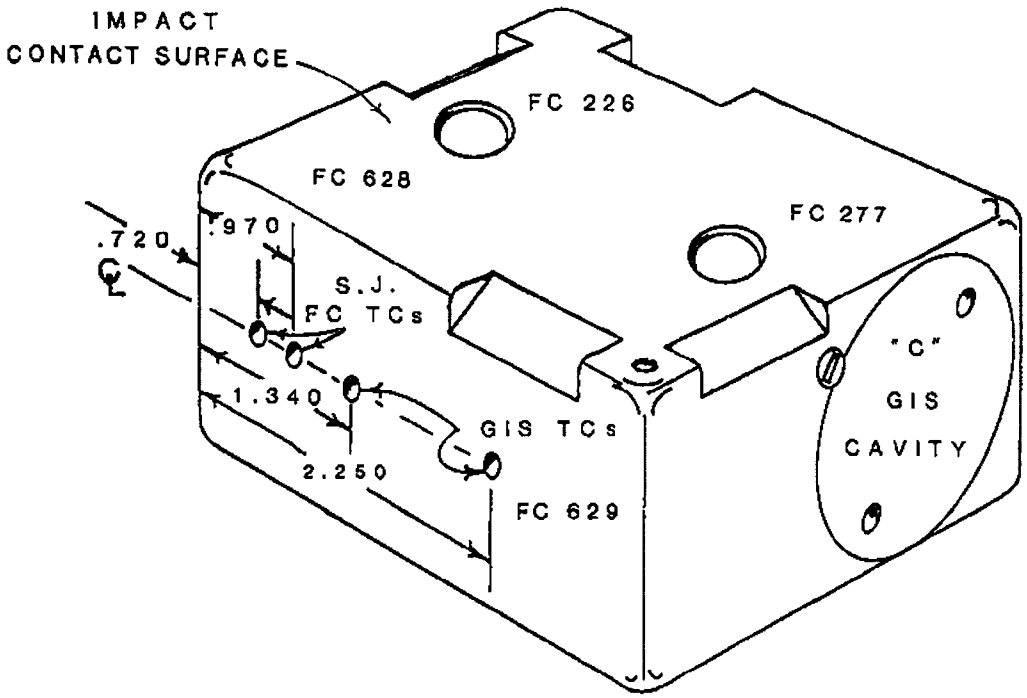

Fig. 28. The SVT-12 impact assembly.

transferred to Wing 2 of the CMR building. Postmortem examination of the test components began on December 20, 1984.

The catch tube was placed in an open-fronted hood and the pump-out plug was removed. A swab was inserted into the pump-out hole and a count taken. Although only low levels of activity were detected, water vapor released by the concrete had condensed on the capsule walls and had reduced the detectable alpha contamination.

The end of the catch tube was removed with some difficulty (the length of the concrete target required pulling the entire lid/concrete assembly out of the hood; only a thin film of water on the concrete prevented contamination of the laboratory). After the lid/target assembly had been transferred to another hood, the inner nickel can (a radiation shield) was removed from the catch tube.

Examination of the catch tube interior revealed that the aeroshell had been completely destroyed (Fig. 29). The aeroshell fractured along the axial contact lines of the GISs and was broken into several small pieces. Aeroshell breakup was the most severe observed to date and reflected the high impact velocity.

Damage to the GISs was similar to that observed in lower velocity impacts. The cap of the primary GIS had been removed, and the impact face of the GIS contained a network of axial cracks running the GIS length (Fig. 30). Although the cap had been removed, the capsule at the closure end of the GIS (FC-628) was not released. The secondary GIS also contained a wide axial crack on the impact face and several small cracks on the other faces (Fig. 31).

The fuel capsules were extracted from the GISs, photographed, and measured. Side and end views of each capsule may be seen in Figs. 32 and 33. Capsule strains are listed in Table X.

Macroscopic examination revealed that the fueled clads at the closure ends of the GISs (FC-628 and FC-226) had breached. The impact face of capsule FC-628 contained a long axial crack (14 mm × 0.1 mm) that traversed the vent and weld shield cups and a short crack (3.3 mm × 0.1 mm) on the vent cup radius (Fig. 32). Capsule FC-226 breached on the trailing face (Fig. 33), with a wide axial crack (15.3 mm × 1.0 mm) that traversed both iridium cups.

Although capsules FC-277 and FC-629 were significantly deformed, no areas of localized iridium deformation were observed in either clad.

E. Bare Clad Impact (BCI) Tests (D. Pavone)

1. BCI-1: Test and Postmortem. In BCI-1, a fueled clad impacted a concrete target at 76.24 m/s and 1090°C. The concrete target had been core drilled from

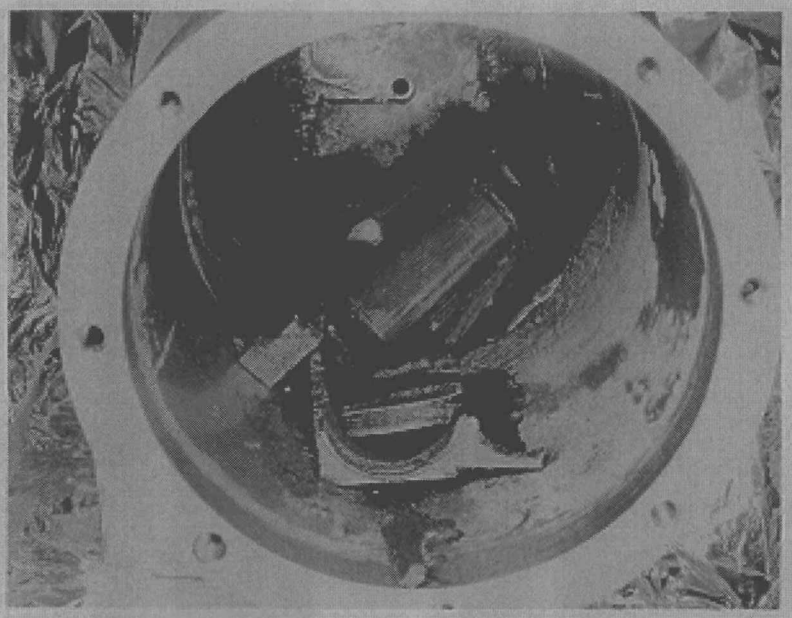

Fig. 29. The SVT-12 aeroshell was badly broken up.

Pad B at the Kennedy Space Center. The test clad (FC-209) was aged 200 h in vacuum at 1287°C and was encapsulated in a welded, tantalum impact can oriented with the cylinder axis parallel to the target face.

The tantalum impact can deformed symmetrically, and the trailing end dished inward to press onto the back of the fueled clad. There was a shallow cylindrical depression on the face of the concrete target.

Photographs of the impacted fueled clad are shown in Fig. 34. An axial breach, ~44 mm long and 9 mm wide, occurred on the back side. The breach extended the full length of the clad. Transverse cracks, ~12 mm × 1 mm and 8 mm × 0.2 mm, were present on the impact face near the cylinder-to-end transition radius. Additionally, a failure occurred along the centerline of the weld bead, ~ 18 mm × 1 mm. An area on the trailing face of the clad, roughly 6 mm × 10 mm, exhibited extensive microcracking and surface spallation. Dark gray surface deposits were also present, suggesting possible contamination by materials used for the impact can hardware.

Metallographic cross sections through the weld failure, the impact can failure, and the area with surface spallation were examined. Figure 35 shows the weld bead microstructure. The offset of the capsule wall on either side of the fracture is indicative of nonuniform strain imposed by differential displacement of large plutonia fragments. The weld penetration was complete, there was no porosity, and the grain structure appeared to be free of transversely oriented columnar grains.

Photomacrographs of the impact face failure on the vent end are shown in Fig. 36. The photomacrographs show that the end of the capsule curled nearly 180° towards the interior. The fracture mode at the failure was intergranular, with no evidence of ductile iridium deformation. However, the generalized reduction in thickness of the capsule wall of about 33% both in the flat impact face and the curled region demonstrates the beneficial effect of compressive stresses normal to the wall thickness. The reduction of thickness indicates that the frictional forces at the plutonia/iridium and iridium/tantalum interface were low enough to permit the iridium to elongate. A narrow intergranular crack progressing from the exterior through about 50% of the thickness suggests that the potential exists for severing a relatively large piece of iridium to create a much larger fracture.

Figure 37 shows the microstructure of a transverse cross section including the surface-spalled area. The microstructure consisted of relatively fine grains elongated in the plane of the capsule wall. Extensive grain boundary fracturing resulted in loss of material from the surface, as well as loss of a few individual grains from the face of the metallographic sample. Longitudinal cracks existed at about two-thirds of the thickness from the exterior surface. There were no tensile stresses normal to the wall thickness during the impact event to account for these fractures, and they perhaps indicate the depth of contaminant penetration.

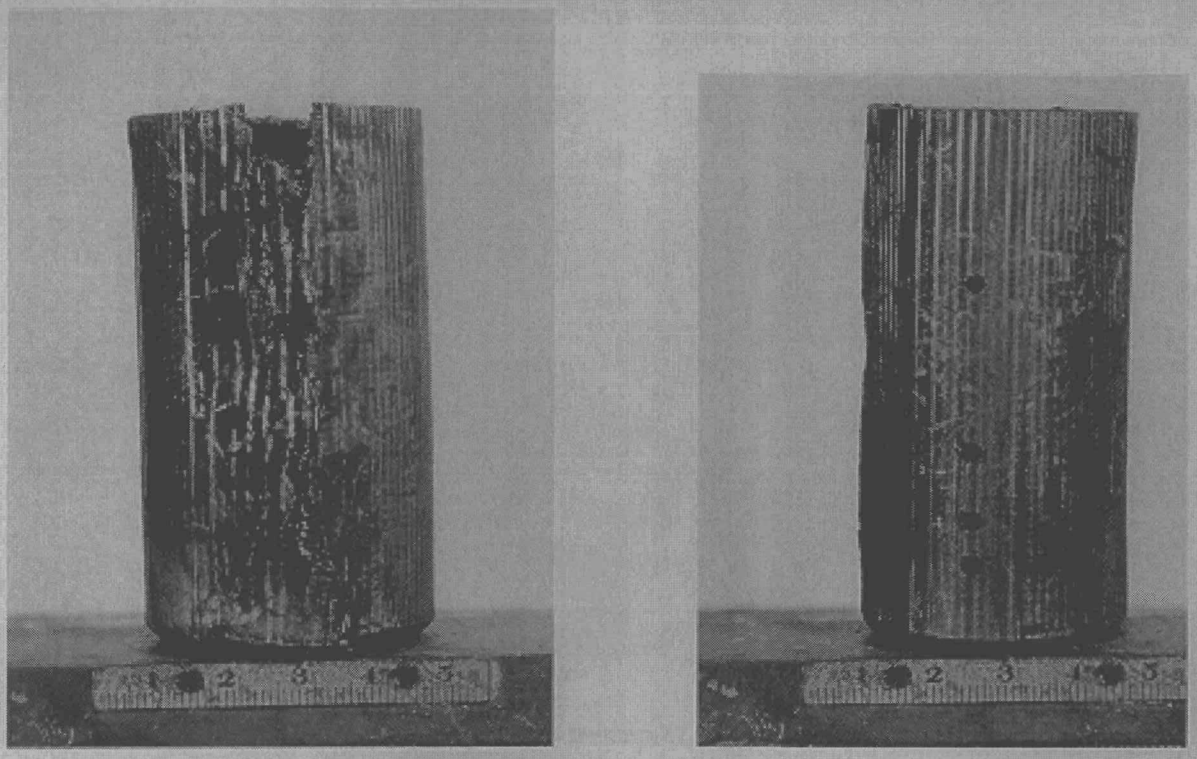

(a) (b)

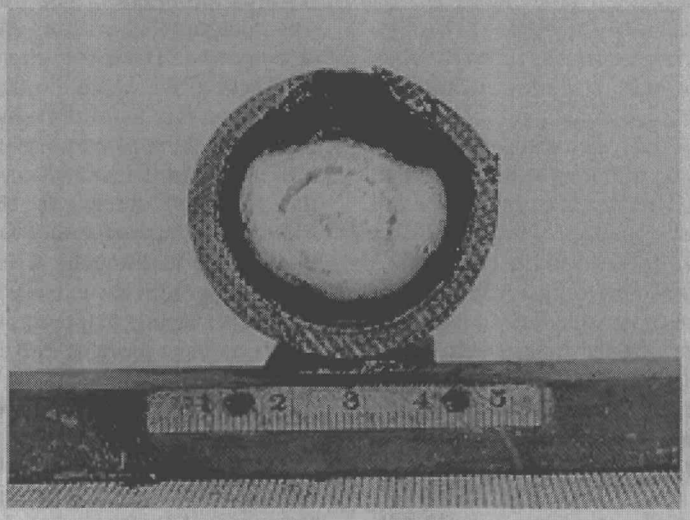

(c)

Fig. 30. The cap of the primary GIS had been removed. (a) Impact face, (b) profile, and (c) closure end; all at 1X.

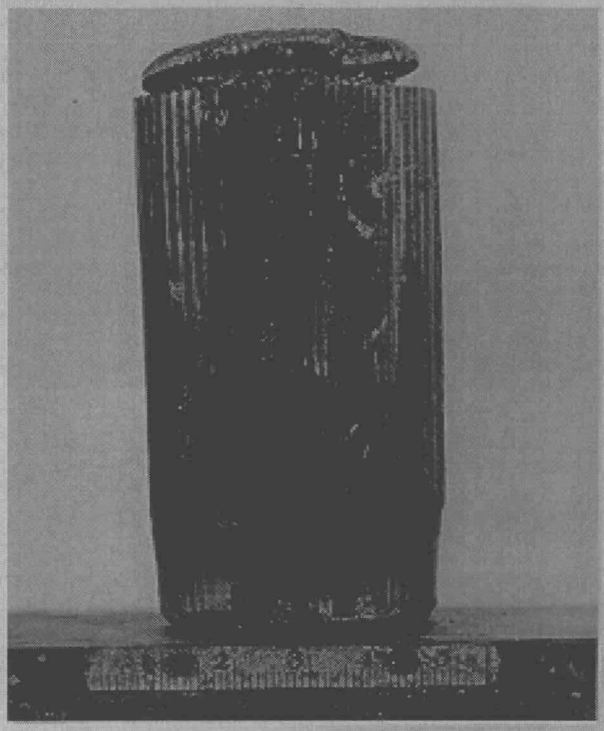

(a)

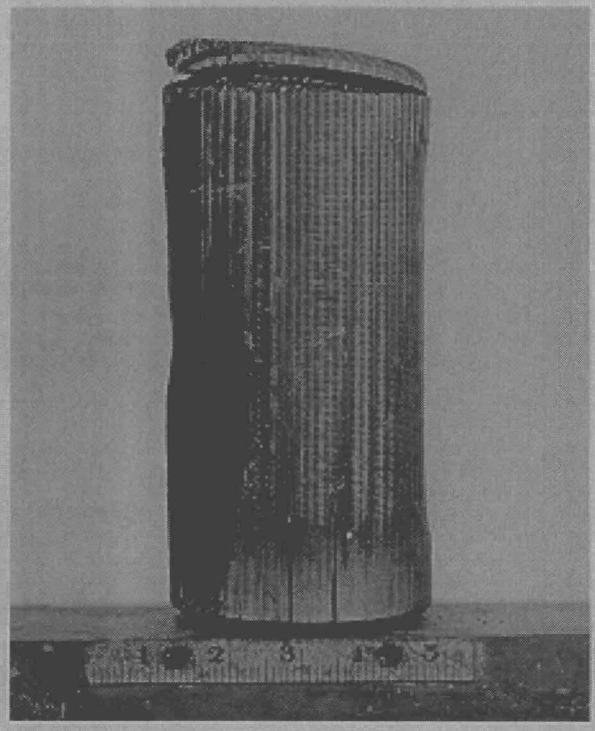

(b)

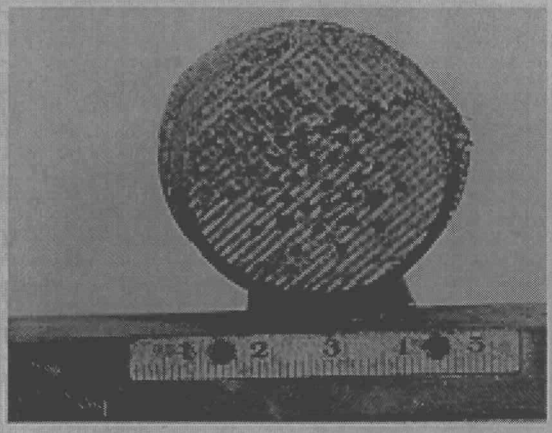

(c)

Fig. 31. The impact face of the secondary GIS contained a wide axial crack. (a) Impact face, (b) profile, and (c) closure end; all at 1X.

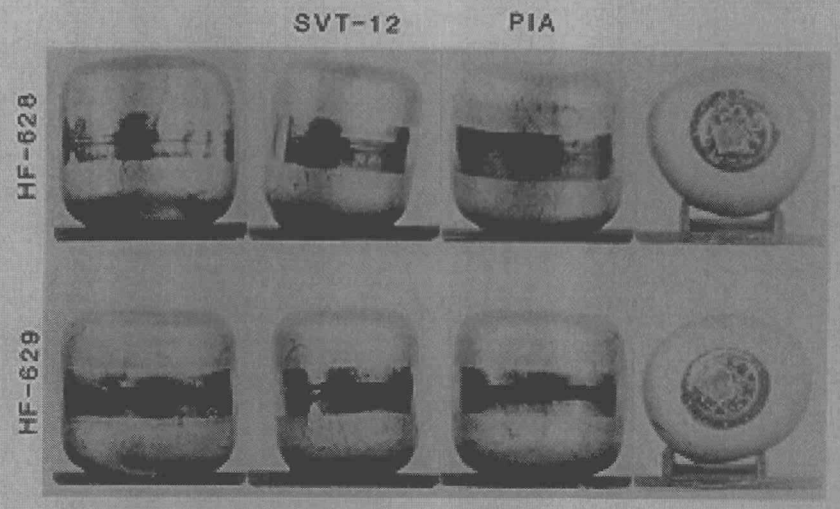

Fig. 32. Clads contained within the primary impact assembly.

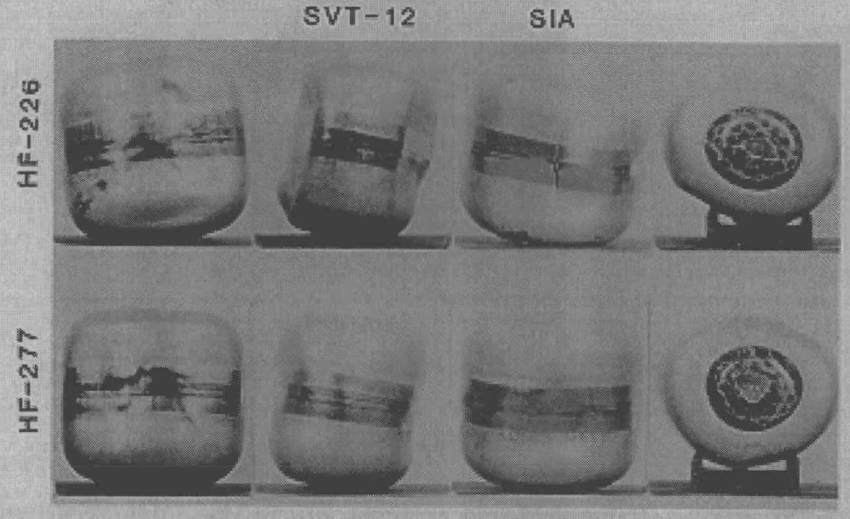

Fig. 33. Clads contained within the secondary impact assembly.

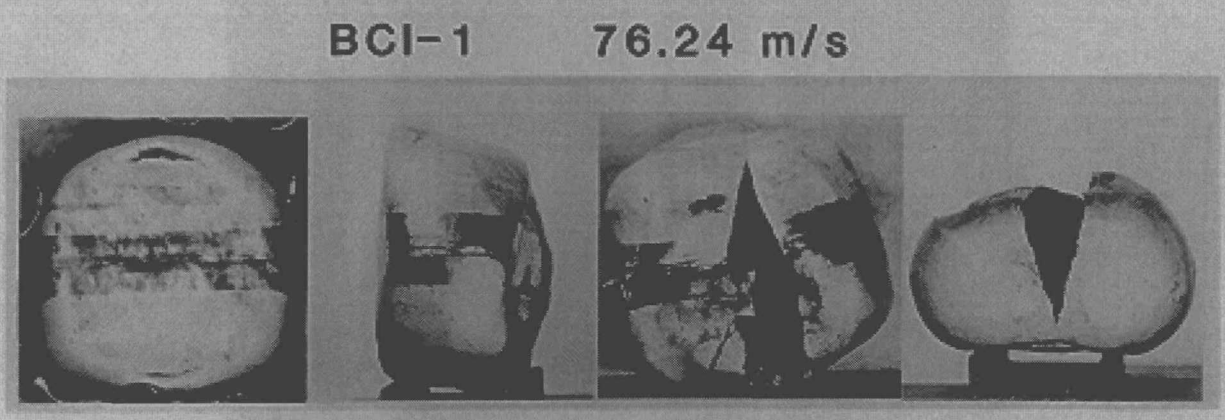

Fig. 34. The iridium clad in test BCI-1 sustained a severe breach on the back, two transverse breaches on the impact face, and a weld failure on the side; ~0.7X.

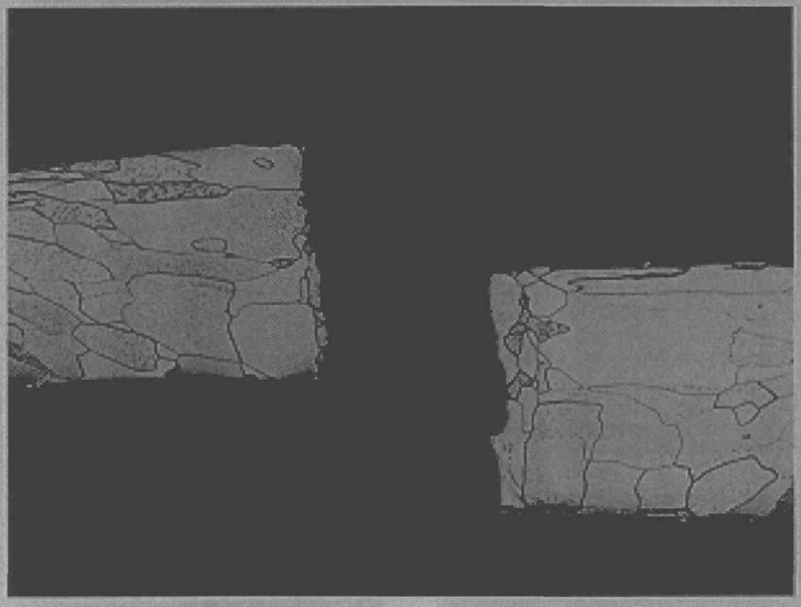

Fig. 35. The offset of the capsule wall on either side of the weld bead fracture of FC-209 indicates nonuniform strain imposed on the iridium capsule wall. The microstructure was acceptable; 50X.

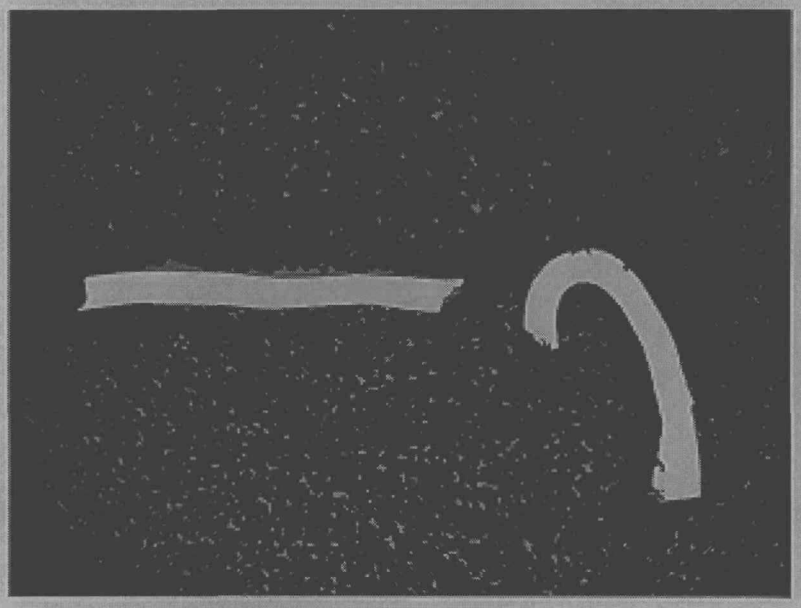

(a)

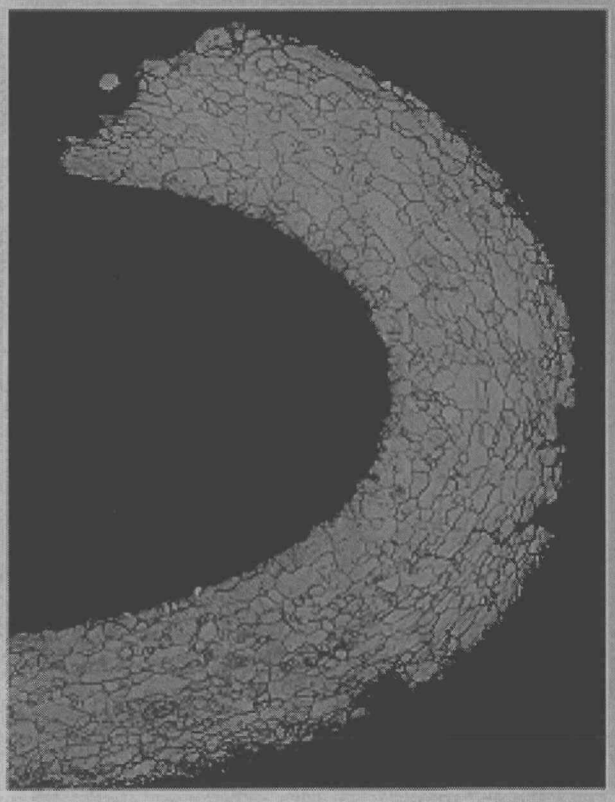

(b)

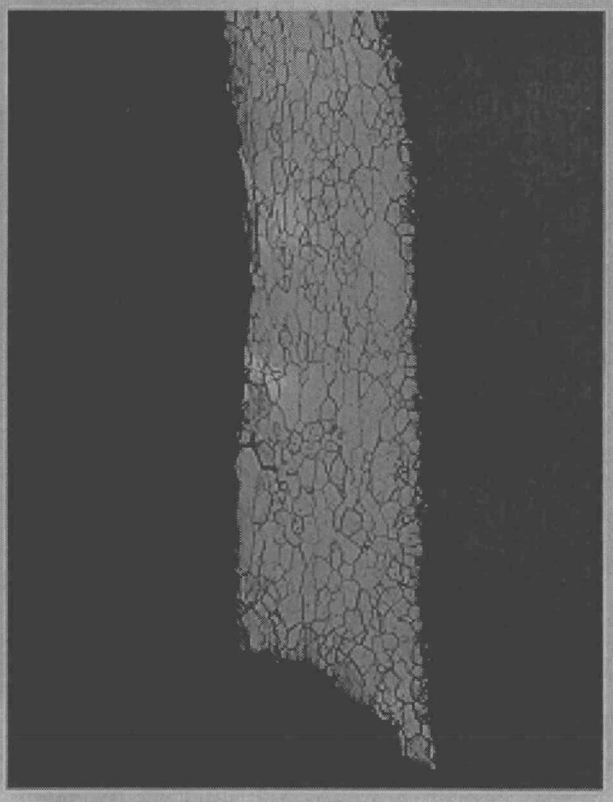

(c)

Fig. 36. Transverse impact face failures in FC-209 resulted from curvature of the capsule end towards the interior of the capsule. (a) 7X; (b) and (c) 50X.

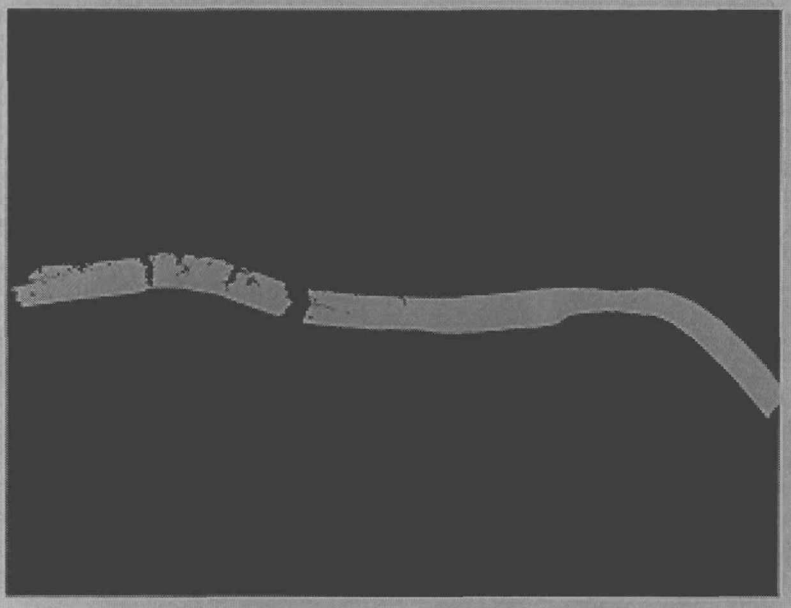

(a)

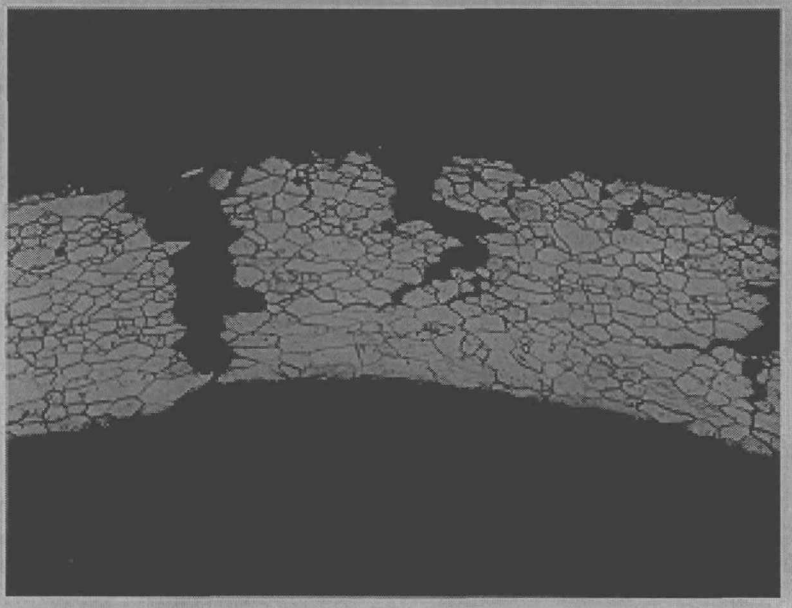

(b)

Fig. 37. Microstructure of the FC-209 capsule wall that exhibited surface spallation. Extensive grain boundary fracturing occurred; (a) 7X and (b) 50X.

Electron microprobe examination of surface deposits on an area exhibiting microcracking showed that the deposits contained tantalum, iron, carbon, and oxygen. The base metal elements, iridium and tungsten, were also detected; however, in some locations, the coating thickness was sufficient to nearly obscure the underlying iridium/tungsten alloy.

AES analysis of the exterior of a fractured sample obtained from an area with surface discoloration revealed very strong peaks for chlorine, oxygen, and copper, as well as lesser concentrations of iron, carbon, silver, and sulfur. A similar spectrum was obtained from the center of the sample; the interior portion had only modest levels of carbon and oxygen and a trace of phosphorus. The AES spectra of a second sample indicated that the grain boundary impurities consisted of modest amounts of carbon, oxygen, and a small amount of phosphorus. These results indicate that the contamination of the iridium was not uniform and that the source of the impurities was outside the clad.

The most likely source of the contaminants was the tantalum hardware, particularly the foils used to fabricate the "saddle" that served to maintain the orientation of the fueled clad. Chlorine, oxygen, and iron may have been present as mill scale on the tantalum foils. Copper could have been introduced from electrodes used to spot weld the fixtures. Although tantalum was present as a constituent of the surface film, it apparently did not diffuse into the grain boundaries.

The weight of plutonia recovered from the impact can was 16.1450 g, and the amount in the <10-μm particle size range was 0.2518 g.

Emission spectrographic analysis of the plutonia pellet (Table VI) showed that all impurities except iron (180 ppm) were present at less than the SRP guideline limit.

In view of the analytical evidence that indicates the iridium capsule was contaminated by extraneous elements introduced with the test hardware, the results of this test should not be considered typical of the fueled clad response.

2. BCI-2: Test and Postmortem. The test clad (FC-214) was aged 200 h at 1287°C. Because of apparent iridium contamination in BCI-1, the tantalum impact can hardware was vacuum outgassed for 1 h at 1250°C before being loaded with the fueled clad and welded. The impact test parameters were 53.7 m/s, 1091°C; a Kennedy Space Center, Pad B, concrete core target was used.

No failures of the iridium clad were observed. A shallow depression was present on the face of the concrete target, and the impact face of the fueled clad was roughened, replicating the concrete target surface. An axial ridge at the location of a fuel fragment push-through was present on the impact face, but the most severe localized iridium deformation occurred at the ends of the impact face. Photographs of the impacted capsule are shown in Fig. 38; test results are summarized in Table XI.

The plutonia fracture pattern is shown in Fig. 39. The pellet fractured into several relatively large fragments; the fracture plane that caused the axial ridge on the impact face was readily apparent. Although the impact target was a rigid material, extensive crushing of the plutonia at the impact face did not occur. Instead, the change in shape appears to have been accommodated primarily by the relative displacement of fuel fragments.

Small transverse cracks were observed on the interior of the iridium clad at the ends of the impact face. The largest of these occurred near the vent end. Figure 40 shows a photomacrograph and a photomicrograph of

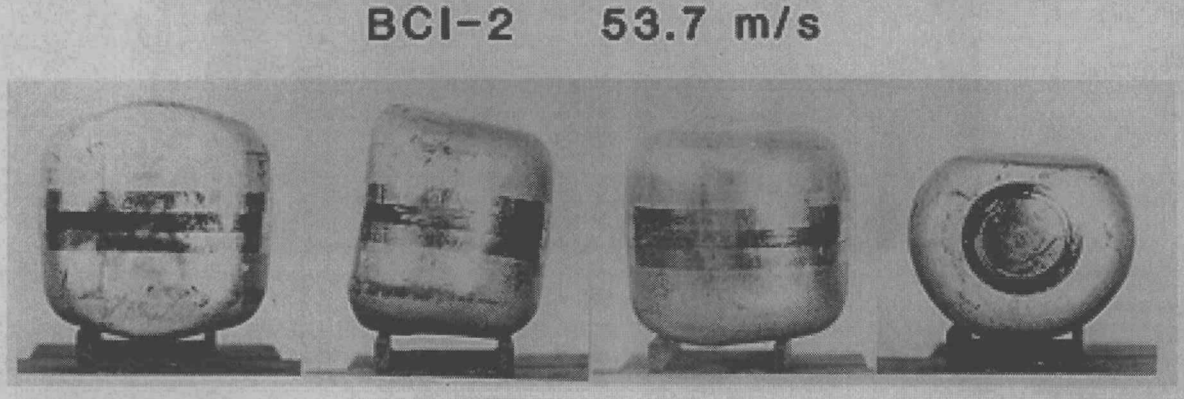

Fig. 38. Photographs of the impacted fueled clad FC-164. There were no failures. Left to right — impact face, side profile, back, and vent end; all at ~0.7X.

Table XI. BCI Test Summaries

Test	Fueled Clad	Clad NDE Value	Velocity (m/s)	Gross Deformation (%)			Failures	Pu Release (g)	
				Diam	Weight	Length		Total	<10 μm
BCI-1	FC-209	2.0	76.24	+31.7	−23.2	+27.0	4	14.2076	0.2215
BCI-2	FC-164	1.4	53.70	+ 9.6	+10.2	+11.2	0	0	0
BCI-3	FC-351	2.1	64.77	+12.3	−10.3	+15.2	2	0.0008	0.0001

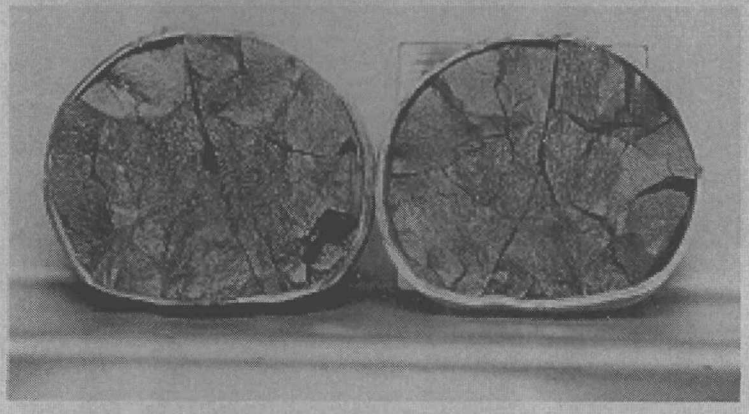

Fig. 39. The plutonia pellet of FC-164 fractured into relatively large fragments. Extensive crushing on the impact face was not observed; ~1.5X.

the metallographic cross section through this region of the capsule. The crack was widest at the interior surface and extended through ~85% of the wall thickness. A secondary crack, extending through ~20% of the thickness, was present near the principal crack. The fracture mode was intergranular with no indication of ductility at the fracture site.

A transverse cross section through a ridge on the impact face is shown in Fig. 41. Mild reverse bending occurred near the site of the fuel fragment indentation. Reduction of thickness at the point of indentation was about 30%. No evidence of cracking was detected in the reverse bend region. Because the impact occurred against a rigid target (concrete), only limited deformation of the iridium was possible and a breach of the capsule was averted. Had the impact occurred with a compressible material such as FWPF graphite between capsule and target, a breach might well have occurred.

The chemical analysis of the plutonium pellet is tabulated in Table VI. Impurity elements are present at levels within the SRP guideline limits.

3. BCI-3: Test and Postmortem. Fueled clad FC-351 was aged 220 h in vacuum and was encapsulated in an outgassed tantalum impact can oriented for impact with the axis parallel to the target face. The impact velocity was 64.77 m/s and the clad temperature was 1090°C. The target was a concrete core removed from a Kennedy Space Center launch pad.

Photographs of the impacted fueled clad are shown in Fig. 42. The impact face had a curved profile corresponding to a shallow depression produced in the target face; the surface replicated the roughness of the concrete. Visual examination revealed that two narrow transverse cracks were present on the shield cup end. The breaches are indicated by arrows in Fig. 42. Severe localized deformation occurred on the vent end of the impact face. Test results are summarized in Table XI.

The plutonia fracture pattern is shown in Fig. 43. There appeared to be a tendency toward the formation of small, elongated, radially oriented fragments around the periphery of the cross section. The remainder of the pellet consisted of relatively large, irregularly shaped

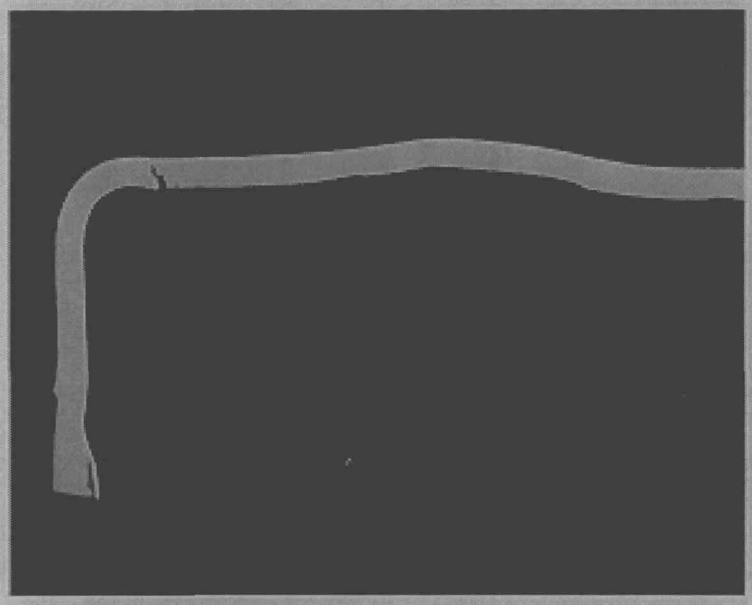

(a)

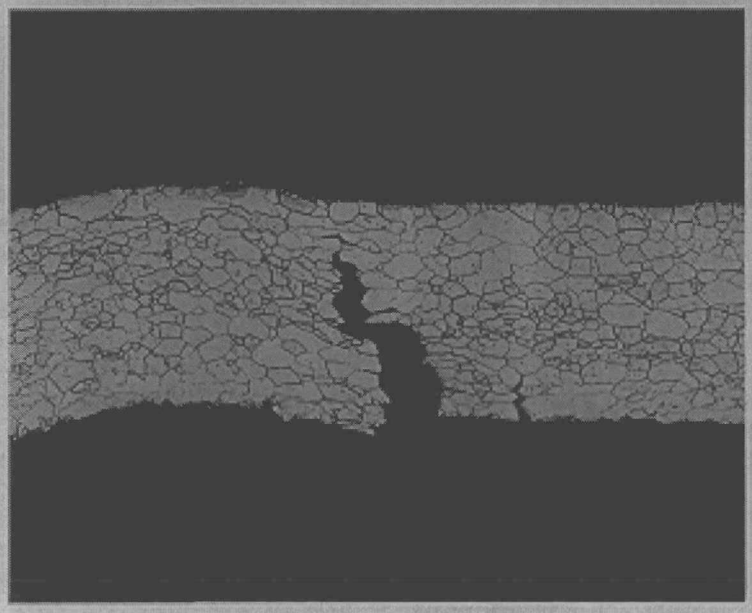

(b)

Fig. 40. A crack was initiated on the interior surface of the iridium at the vent end of the impact face. (a) 6.5X and (b) 50X.

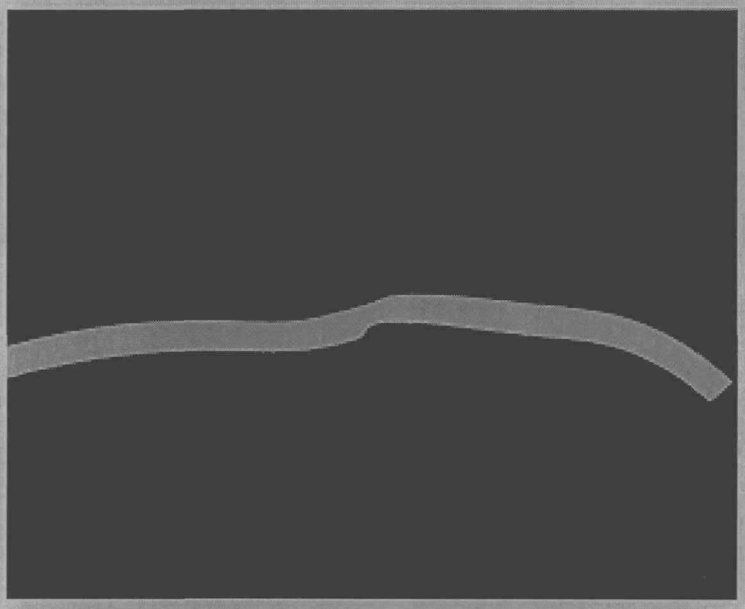

(a)

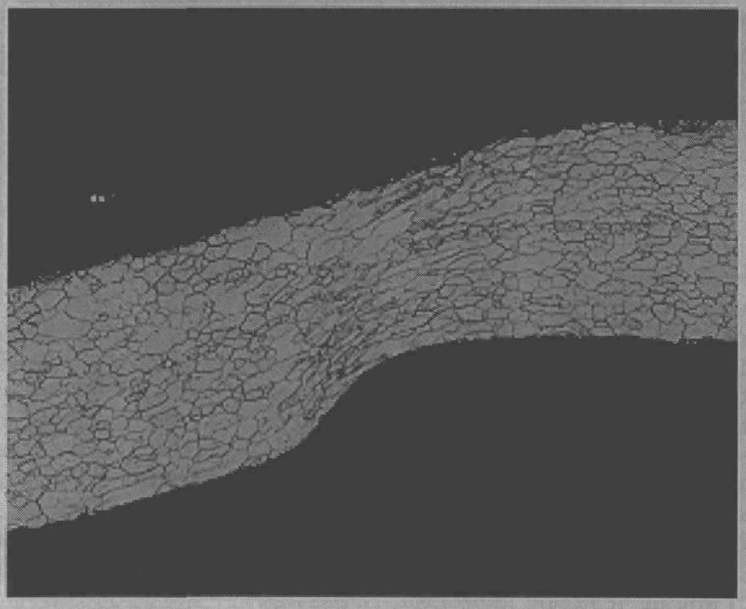

(b)

Fig. 41. Fuel fragment push-through caused an axial ridge on the impact face in BCI-2. The iridium was supported by the rigid target and did not breach; (a) 6.5X and (b) 50X.

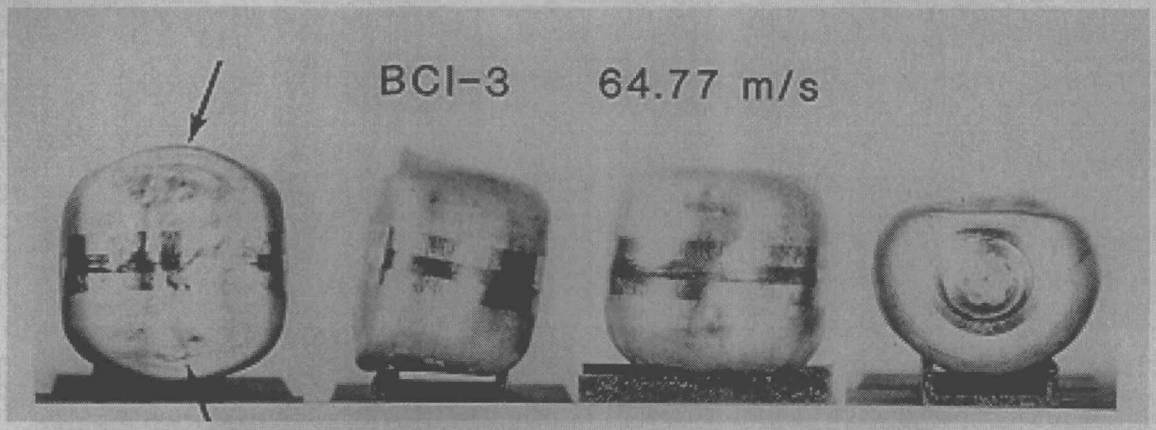

Fig. 42. Transverse cracks at the ends of the impact face occurred in FC-351. Left to right—impact face, side profile, back, vent end; all at 0.7X.

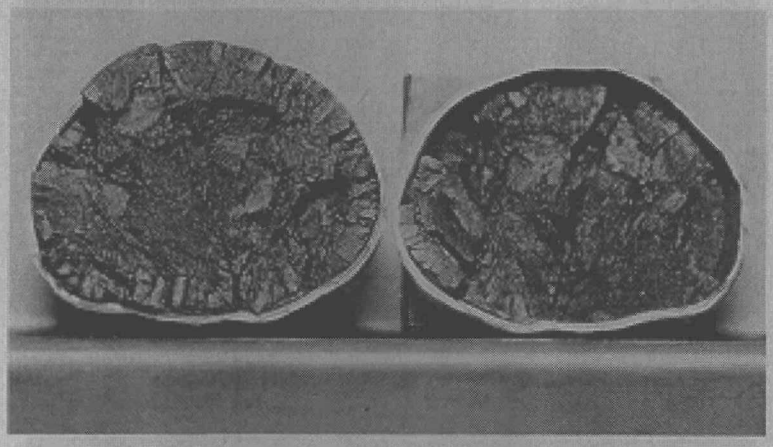

Fig. 43. The plutonia fracture pattern of FC-351 exhibited a tendency to form small, radially oriented fragments on the periphery, although the principal fracture mode was large, irregularly shaped fragments; ~1.5X.

fragments. Similar to the pellet in BCI-2, the impact face of the pellet was not severely crushed.

Metallographic examination of a longitudinal cross section cut from the vent end of the impact face showed three penetrating cracks. Consistent with previous observations, the fractures were widest at the interior surface of the capsule wall. One of the fractures barely penetrated the capsule wall. The fractures were all intergranular with no evidence of localized ductility (Fig. 44). No evidence of failure was observed on the capsule radius.

The plutonia released into the tantalum impact can was recovered by ultrasonic cleaning in water, particle-sized into two fractions, and each fraction analyzed for plutonium content. The total plutonium content of the >10-μm fraction was 0.0007 g, and that of the <10-μm fraction was 0.0001 g.

Impurity elements in the plutonia pellet were all present in amounts below the SRP guideline (Table VI).

F. Bullet/Fragment Test Series

1. Bullet/Fragment Test No. 3: Postmortem Examination (T. George). The test conditions, module disassembly, and preliminary results were described in previous reports. In this quarter, we continued with our investigation of Ir:Al interactions and received the results of microprobe analyses conducted on an intermetallic deposit attached to the Al 2219 bullet.

Microprobe analysis of the deposit cross section (Fig. 45) indicated the apparent presence of several Ir/Al/η phases:

- 96% Al/4% Ir
- 47% Al/53% Ir
- 46% Al/12% Ir/32% Cu/8% Fe/2% Mn
- 30 to 38% Al/70 to 62% Ir
- 27 to 31% Al/73 to 69% Ir

(all values are wt %)

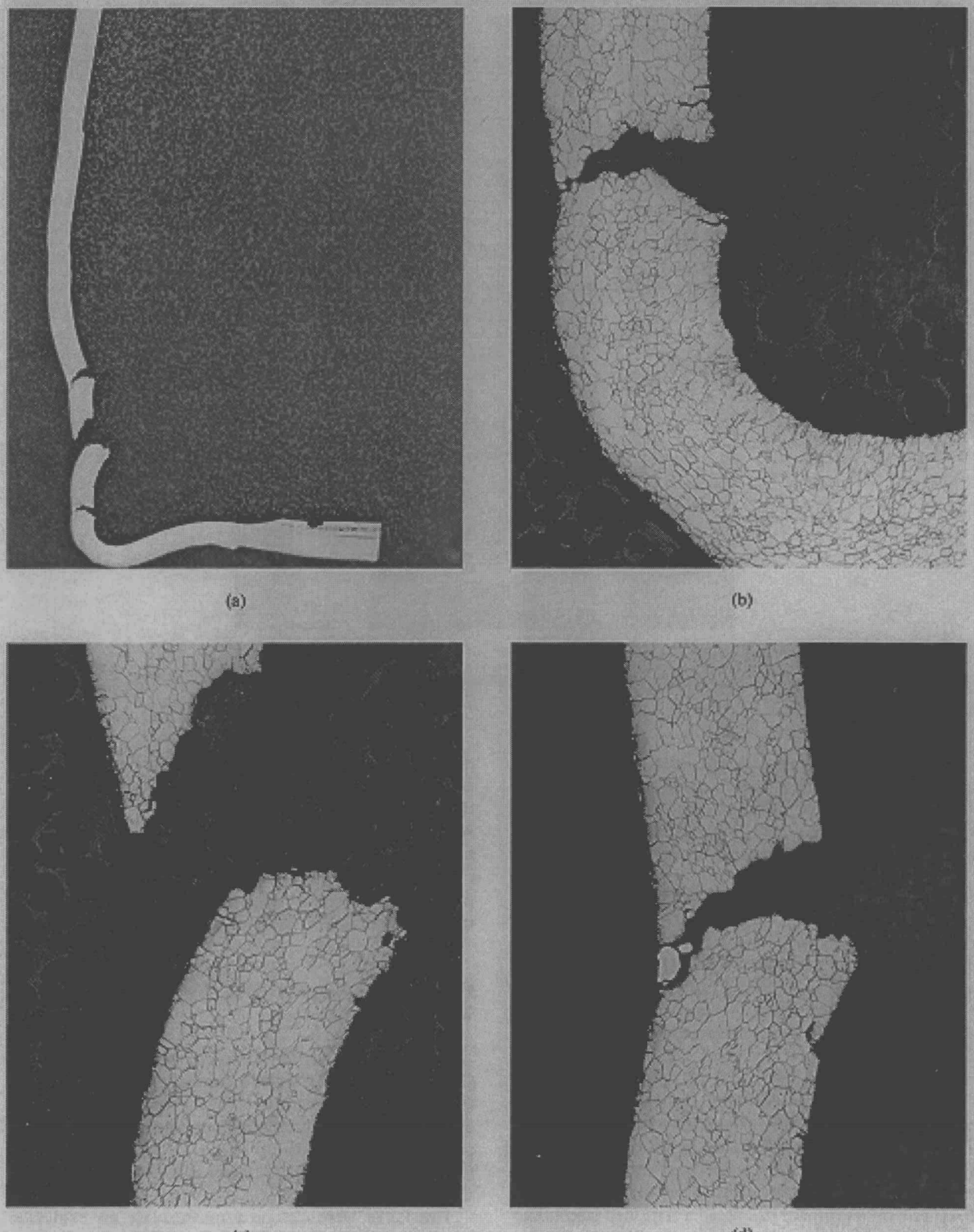

Fig. 44. Three transverse impact face cracks were present on the vent end of the impact face of FC-351; (a) 6.5X; (b), (c), and (d) 50X.

Fig. 45. Optical metallography revealed several phases on a cross section of the intermetallic blob; 40X.

Results of analyses at specific areas on the deposit cross section are presented in Table XII. The 27 to 31% Al/78 to 69% Ir compositional range was particularly interesting because electron imaging of an area with this composition revealed three distinct phase regions.

2. Bullet/Fragment Test No. 5: (R. Tate). In October, we completed the fifth bullet/fragment test. The desired test conditions were a module temperature of 1091°C and a .50-caliber, 18-g, 2219-T87 aluminum alloy bullet at 549 m/s (1800 ft/s). The bullet struck the GPHS half-module about 13 mm to the left of the module centerline and approximately midway between the weld and the top of the clad. The aluminum bullet was deflected by the target, did not come to rest within the assembly, and presumably caused the exit hole observed in the top of the furnace used to heat the target. The module temperature was measured as 1120°C at the time of bullet impact. The velocity of the bullet in this test was determined from a flash x ray at 555 m/s (1820 ft/s). The bullet impact produced a flattened clad plane set at about 60 degrees from the bullet flight path (Fig. 46). Field inspection of the target clad did not indicate a breach of the iridium clad containment. However, closer inspection of the clad in the laboratory revealed a narrow, 3.6-mm-long crack along the weld centerline in the weld overlap region. This crack is shown in Fig. 47. A second crack, a semicircular opening 0.2 mm wide and 4.5 mm long, was observed in the cup radius of the clad adjacent to the bullet impact area. This feature is pictured in the upper left-hand area in Fig. 48 and at higher magnification in Fig. 49.

G. Converter Segment Tests (CSTs) (T. Cull and R. Tate)

In this quarter, we continued to make progress in the CST series. Four tests were conducted: an engineering test to evaluate the response of test hardware and suitability of the test configuration (705-psi static overpressure), CST-1 (736-psi static overpressure), CST-2 (1028-psi static overpressure), and CST-3 (1684-psi static overpressure).

The CSTs were designed to simulate an explosive event in which the radioisotope thermoelectric generator (RTG) housing, insulation, and thermoelectric elements are driven into the GPHS module stack. In

Table XII. Phases in an Intermetallic Deposit Formed in SVT Bullet Test No. 3

Area*	Number of Phases Observed	Approximate Phase Compositions (wt. %)	
1	3	46% Al: 12% IR: 32% Cu: 8% Fe: 2% Mn 96% Al: 4% Ir 47% Al: 53% Ir	
2	4	45% Al: 15% Ir: 32% Cu: 8% Fe 38% Al: 61% Ir: 1% Cu 96% Al: 4% Cu 48% Al: 52% Cu	
3	3	46% Al: 15% Ir: 31% Cu: 8% Fe 38% Al: 62% Ir 97% Al: 3% Cu	
4	2	38% Al: 62% Ir 31% Al: 68% Ir: 1% Cu	
5	3	28.2% Al: 71.8% Ir 27.8% Al: 72.2% Ir 30.2% Al: 69.8% Ir	electron imaging revealed each composition as a distinct phase

*A micrograph of the deposit cross section, showing the five areas of interest, may be seen in Fig. 45.

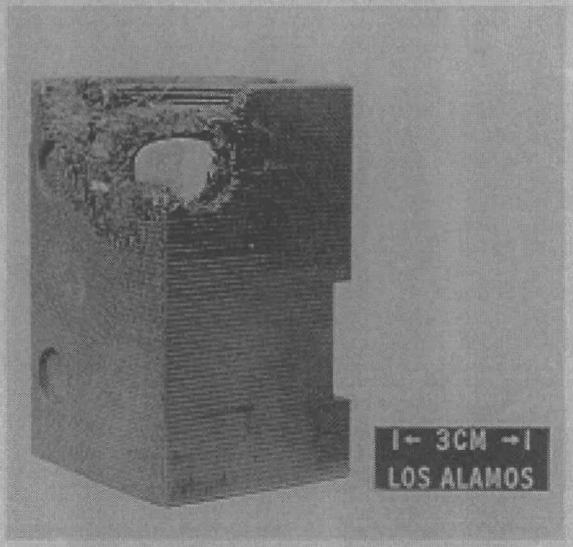

Fig. 46. Fifth bullet test on GPHS half-module after impact by .50-caliber aluminum alloy bullet at 555 m/s (1820 ft/s).

Fig. 47. Crack in the weld seam of the simulant-fueled GPHS clad after bullet impact at 555 m/s; 11X.

Fig. 48. Targeted GPHS fuel clad after bullet impact at 55 m/s. Note semicircular crack in upper left corner.

Fig. 49. Enlarged view of crack in the cup radius area of the targeted GPHS fuel clad after bullet impact; 11X.

each CST, the test object was a flight-quality GPHS module containing four simulant-fueled ($^{238}UO_2$) clads. The module was placed between two bulk graphite modules and suspended in the shock tube by a graphite cradle. The 22-in. I.D. shock tube was purged with a 10-cfh flow of nitrogen, and the module stack was heated to 1091°C (the operating temperature of an on-pad RTG); a 5-cfh flow of nitrogen was maintained in the furnace during module heat-up. When the module stack reached 1091°C, the firing sequence was initiated. At T-25 s, a low-energy explosive pin was detonated, causing the furnace to drop away from the module array. The furnace support then activated a limit switch that sent power to an electric winch to close a sliding door over the withdrawn furnace. Mounted on the sliding door was an RTG housing simulant supported by an aluminum angle frame. The housing simulant consisted of a C-shaped, 0.25-in.-thick aluminum plate, supporting a 3 × 6.8-in. RTG segment (Fig. 50), manufactured by General Electric (GE) (nominal weight = 356 g). The GE converter segment was positioned 1.5-in. upstream from the test module after the sliding door was closed and the winch was deactivated. The test setup is illustrated in Fig. 51. After verifying furnace drop and door closure (by viewing the shock tube on a video monitor), the Comp C-4 explosive was detonated. The test objects were thrown into a vermiculite-filled catch tube approximately 14 ft from the muzzle end of the shock tube. These items were recovered the following day by sifting the vermiculite through 0.125-in. screens. Flash x-ray units were set up to capture the simulant-fueled clads in flight between the shock tube and the catch tube. The purpose of the x rays was to observe particle dispersion, should the clads breach, and estimate the fuel clad velocities from their position on the x-ray films.

Results of the individual CSTs and the engineering test are summarized below.

1. CST Engineering Test. A preliminary engineering test was conducted at Sandia National Laboratories/Coyote III Test Site on October 12 to determine the movement of a flat, circular, 0.25-in.-thick aluminum plate. The 21.5-in.-diam plate, a simulant RTG housing, was supported by an aluminum angle frame designed to allow the plate to move forward freely a distance of 3.5 in. In an actual test, the plate would impact a module array before interacting with the support frame. Two high-speed, 20,000 frames/s cameras viewed the left and right sides of the plate to determine the plate's movement (Fig. 52). Data and results from this test are summarized in Table XIII.

2. CST-1. The first CST was conducted at Coyote Test Site on November 1, 1984. The module array was heated to 1120°C to allow for cooling after the furnace was dropped, but the thermocouple measured no drop in temperature during the 25 s before the high explosive

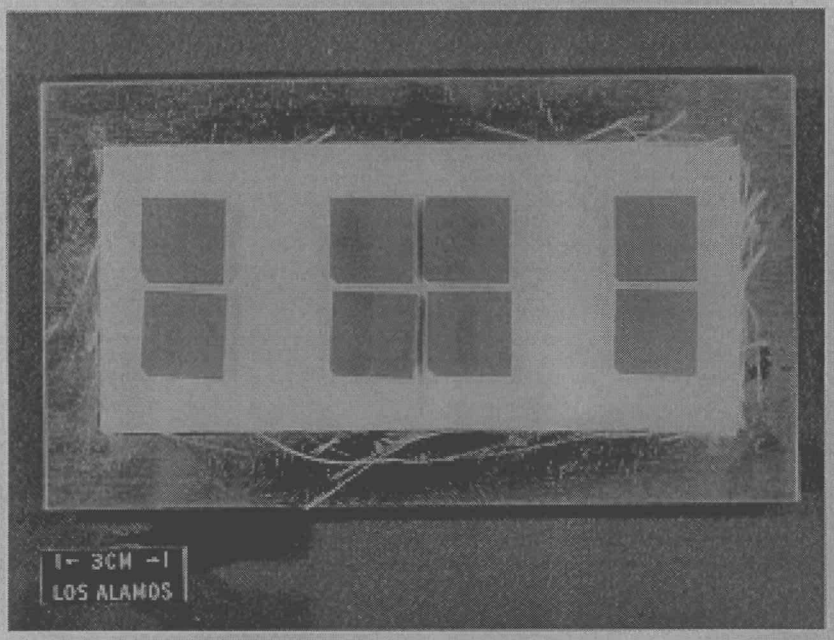

(a)

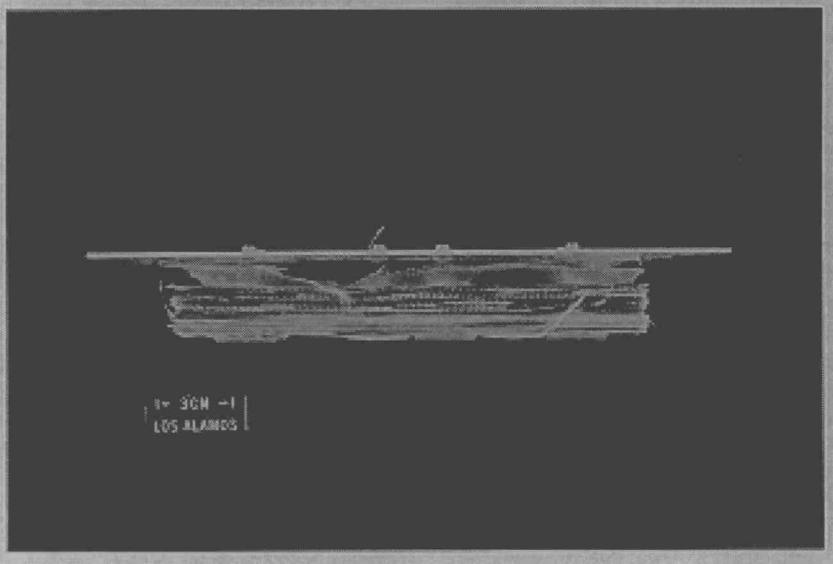

(b)

Fig. 50. GE converter test segment.

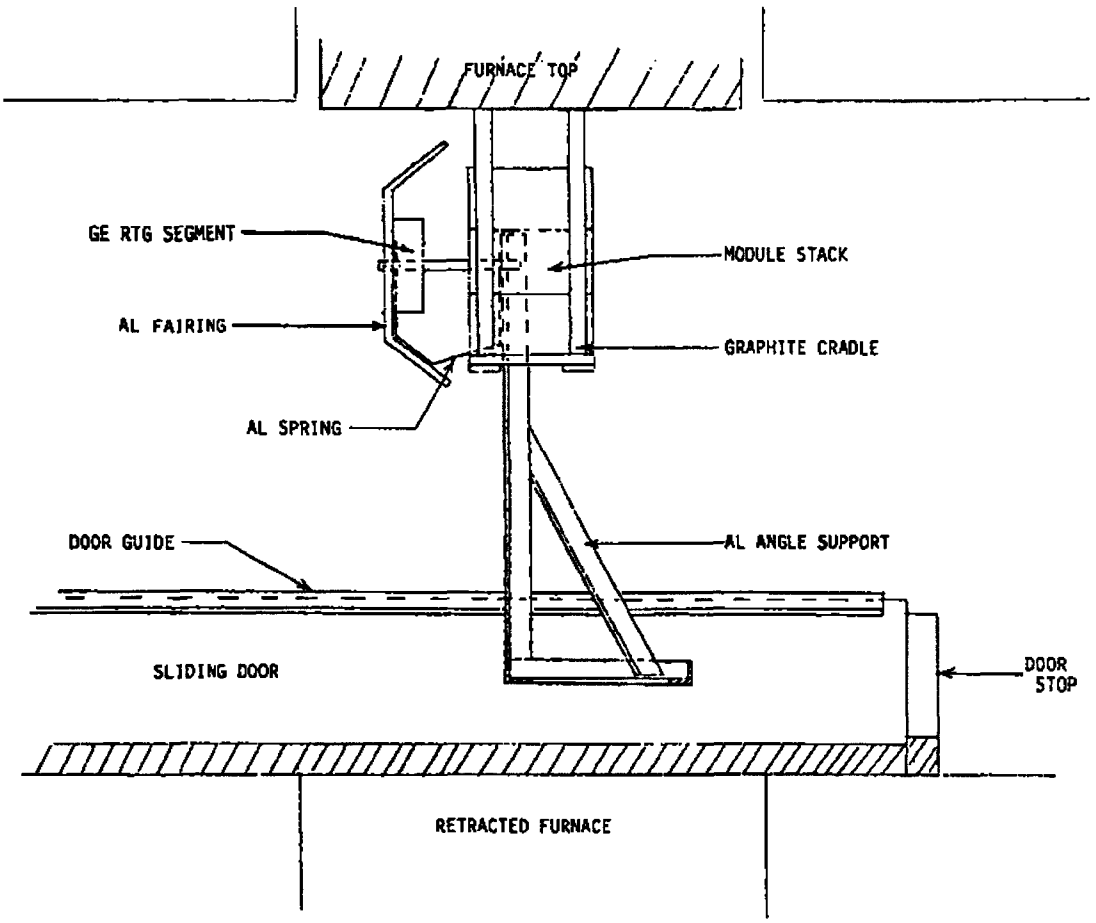

(a)

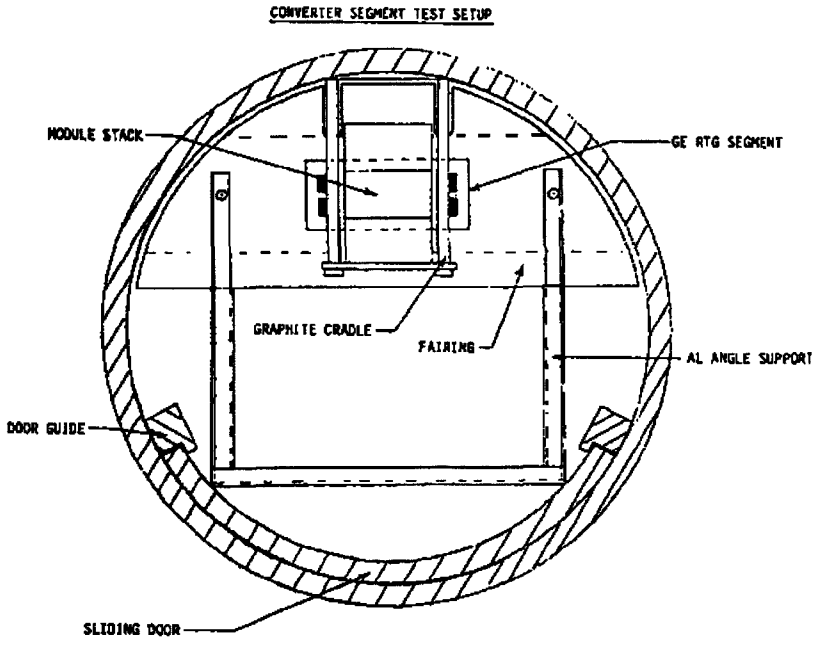

(b)

Fig. 51. CST test configuration. (a) Section view and (b) end view.

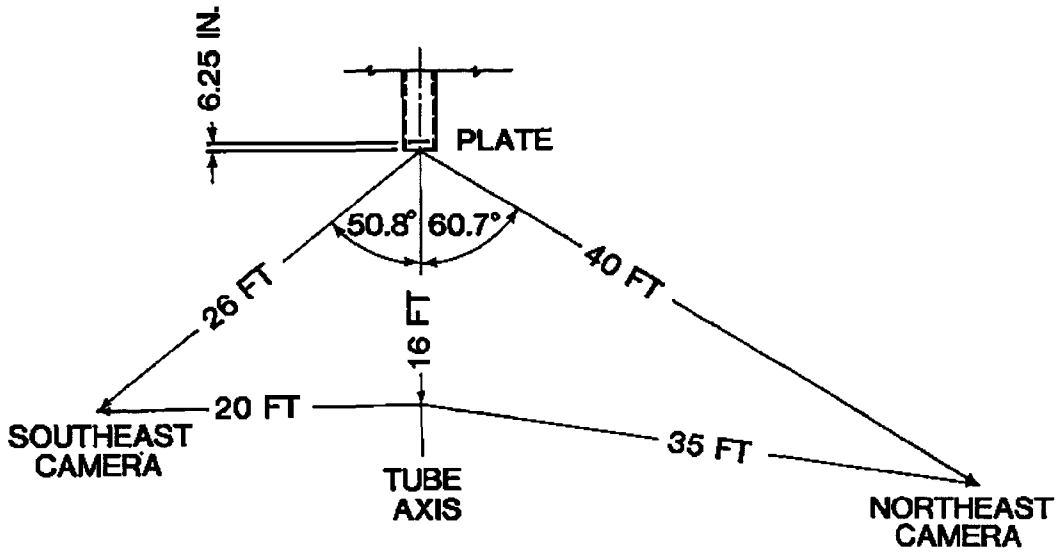

Fig. 52. Camera positions for engineering shock tube test.

was detonated. A shock wave with static overpressure of 736 psi and static impulse of 3.2 psi · s was generated with 60 lb of Comp C-4 explosive. None of the clads breached, but all were deformed. Posttest diametral measurements of the fuel clads are listed in Table XIV. Posttest identification of specific fuel clads was not possible, so the clads were labeled Nos. 1, 2, 3, and 4 in the order they were recovered. Figures 53 and 54 show the deformed clads. Data and results from this test are summarized in Table XIII.

3. CST-2. The second CST was conducted on November 28, 1984, at Coyote Test Site. An identical test setup was subjected to a static overpressure of 1028 psi and a static impulse of 3.75 psi · s. The clads were again deformed, but none breached. Posttest diametral measurements of the fuel clads are listed in Table XIV. Posttest identification of the fuel clads was made possible by comparing pretest and posttest photographs of the clad vents. Figures 55 and 56 show the deformed fuel clads. Data and results from this test are summarized in Table XIII.

4. CST-3. A third shock tube test with a test setup identical to CST-1 and CST-2 was conducted on December 10, 1984, at Coyote Test Site. The GPHS-RTG segment was subjected to a static overpressure of 1684 psi · s and a static impulse of 4.2 psi · s. The clads were again deformed, but not breached. Posttest diametral measurements are listed in Table XIV. Laser etchings on each fuel clad made posttest identification of the fuel clads possible. The resulting damage to the fuel clads is shown in Figs. 57 and 58. The shock tube end was bulged and, therefore, was not reusable. Data and results are summarized in Table XIII.

II. SAFETY TECHNOLOGY PROGRAM

A. Ir/Th and Ir/P Compounds (J. Archuleta)

Methods of growing Ir/Th and Ir/P single crystals within a copper melt were discussed in previous reports. In November, we used the scanning electron microscope (SEM) to photograph Ir/Th and Ir/P single crystals grown with this technique (Figs. 59 and 60). The micrographs clearly illustrate the respective structures of the two crystals.

B. Characterization of the Al/Ir Binary System (K. Axler and L. Foltyn)

1. Phase Identificaton. Study of the Al/Ir system continued during this quarter. A sample of 3:1 at.% Ir:Al was prepared in the arc melter and analyzed by x-ray diffraction (XRD). The x-ray analysis indicated that the 3:1 mixture melted to form IrAl and unreacted iridium. The presence of unreacted iridium implies that no compounds exist on the iridium-rich side of the Ir/Al binary phase diagram. However, the rapid cooling provided by the arc melter does not allow sufficient time for equilibrium to be achieved as a melt cools. Consequently, we divided the original XRD sample into two specimens;

TABLE XIII. CST Summaries

Test	Overpressure (psi)[a]			Temp (C°)	Test Unit	Catch Tube Penetration (ft)	Results
	Static	Reflected	Static Impulse				
CST-ENG	705 ± 70	5189	3.2 ± 0.4	25	RTG Housing Simulant	10	Simulant shattered into 50+ pieces
CST-1	736 ± 70	5434	3.2 ± 0.4	1120	GPHS Module	8	Graphite stripped from clads; slight clad deformation
CST-2	1028 ± 100	NP[b]	3.75 ± 0.5	1054	GPHS Module	11	Graphite stripped from clads; slight clad deformation
CST-3	1684 ± 300	NP	4.2 ± 0.8	1084	GPHS Module	21	Graphite stripped from clads; moderate clad deformation

[a]Figures provided by Sandia National Laboratories.
[b]No information provided by Sandia National Laboratories.

TABLE XIV. CST Capsule Strains

Test	Clad No.	Position	Avg. Major Diam (in.)	Avg. Minor Diam (in.)	Major/Minor Ratio
CST-1	1	ND[a]	30.564	28.604	1.069
	2	ND	30.420	29.366	1.036
	3	ND	30.661	28.682	1.069
	4	ND	30.111	29.456	1.022
CST-2	2	GIS C-OE	30.569	28.903	1.059
	4	GIS C-BE	30.753	29.032	1.059
	1	GIS A-BE	30.264	29.417	1.029
	3	GIS A-OE	29.918	29.389	1.018
CST-3	L-12	GIS A-BE	30.209	27.974	1.080
	L-14	GIS A-OE	30.378	28.025	1.084
	L-16	GIS C-BE	30.742	27.635	1.113
	L-19	GIS C-OE	30.048	28.575	1.052

[a]Not determined.

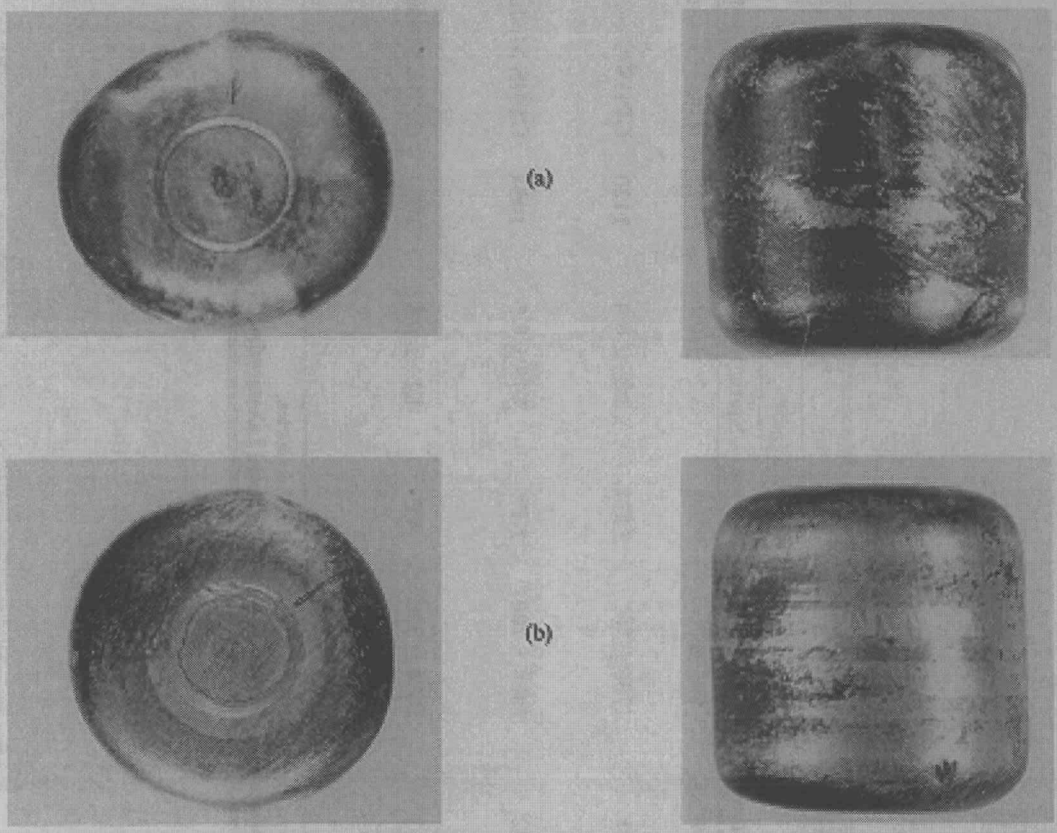

Fig. 53. CST-1 fueled clads 1 and 2, vent end and side views. (a) Fueled clad 1 and (b) fueled clad 2.

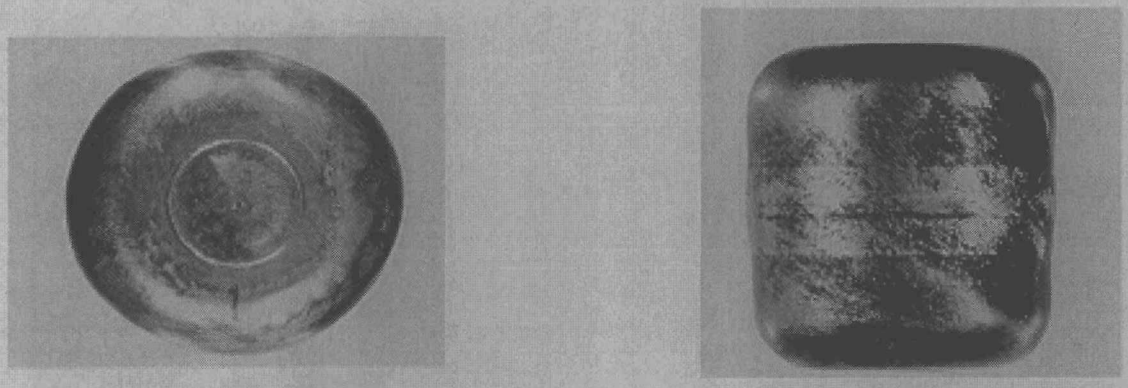

(a)

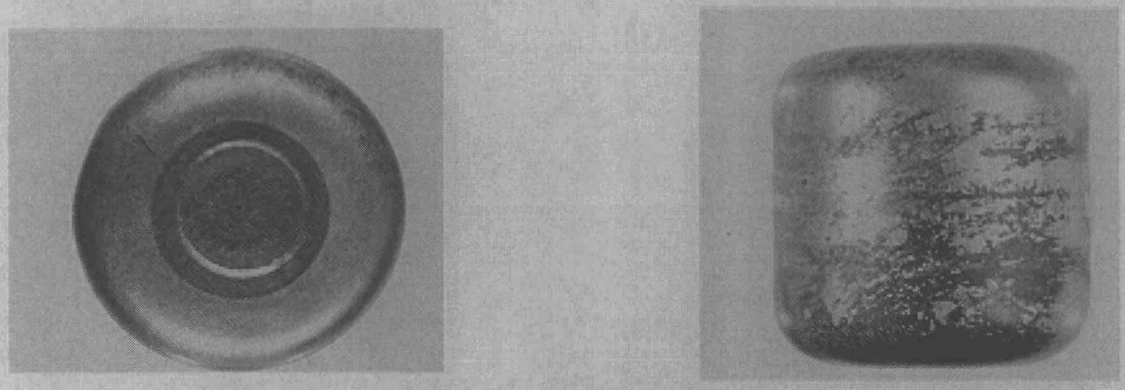

(b)

Fig. 54. CST-1 fueled clads 3 and 4, vent end and side views. (a) Fueled clad 3 and (b) fueled clad 4.

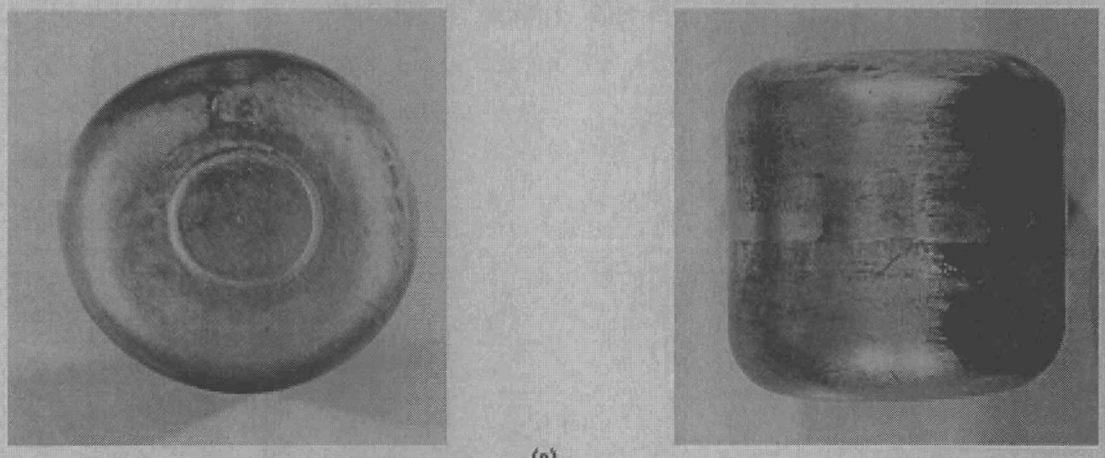

(a)

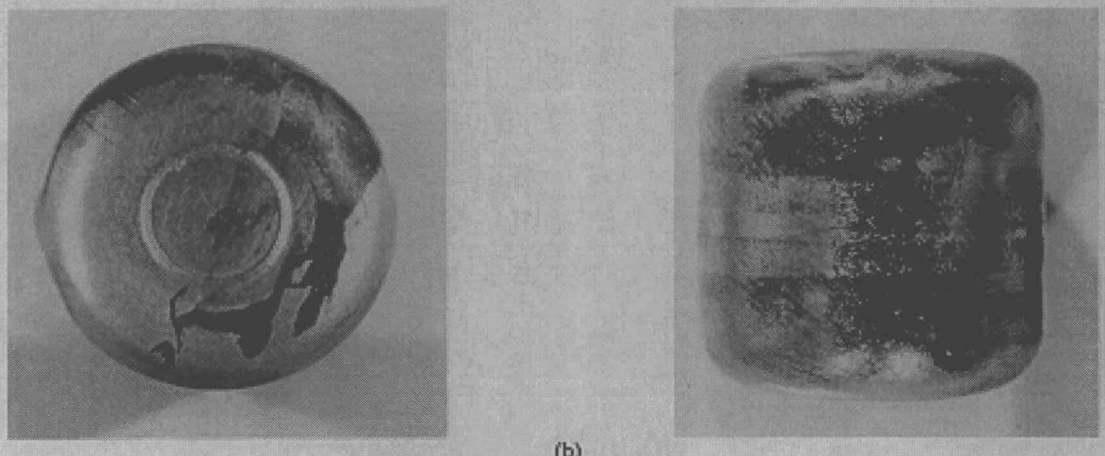

(b)

Fig. 55. CST-2 fueled clads 1 (A GIS, blind end) and 2 (C GIS, open end), vent end and side views. (a) Fueled clad 1 and (b) fueled clad 2.

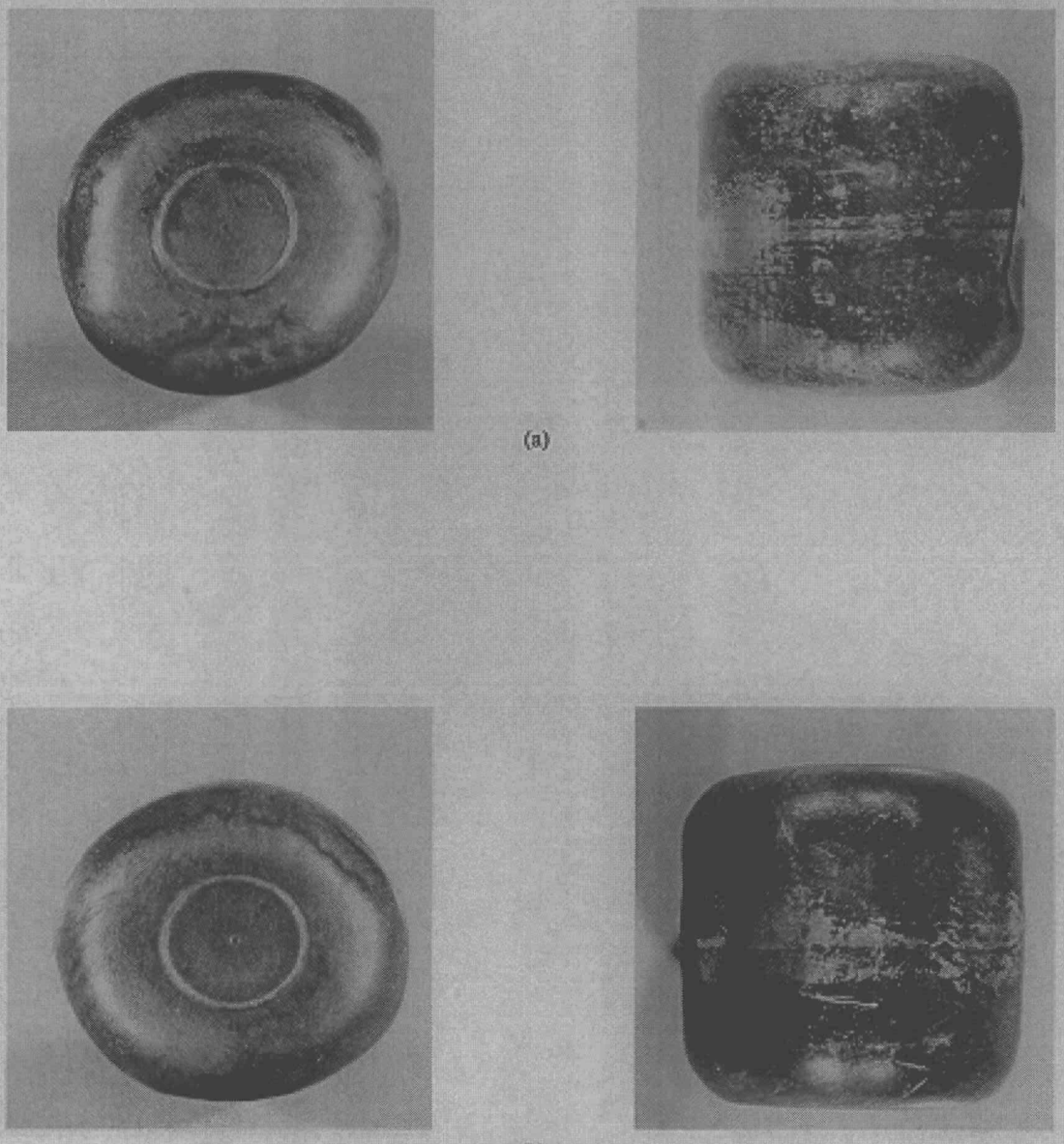

Fig. 56. CST-2 fueled clads 3 (A GIS, open end) and 4 (C GIS, blind end), vent end and side views. (a) Fueled clad 3 and (b) fueled clad 4.

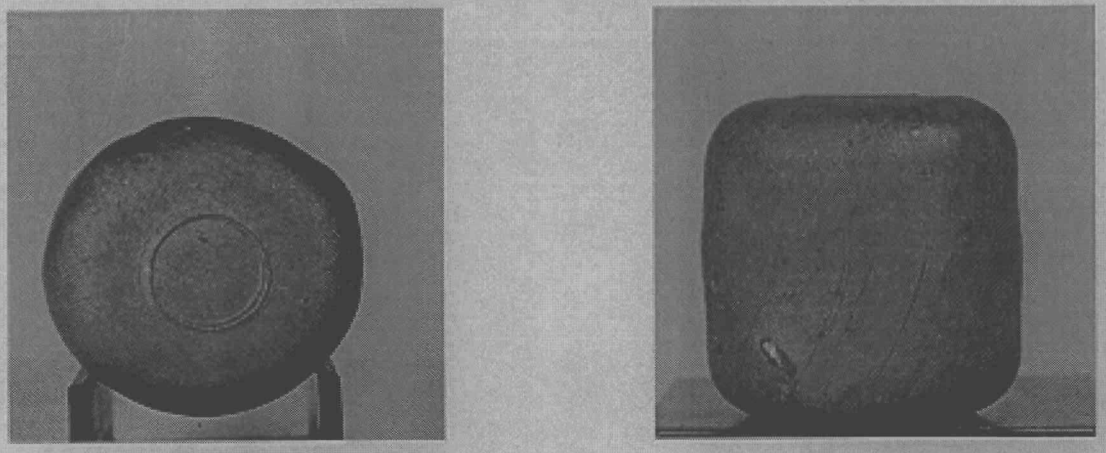

(a)

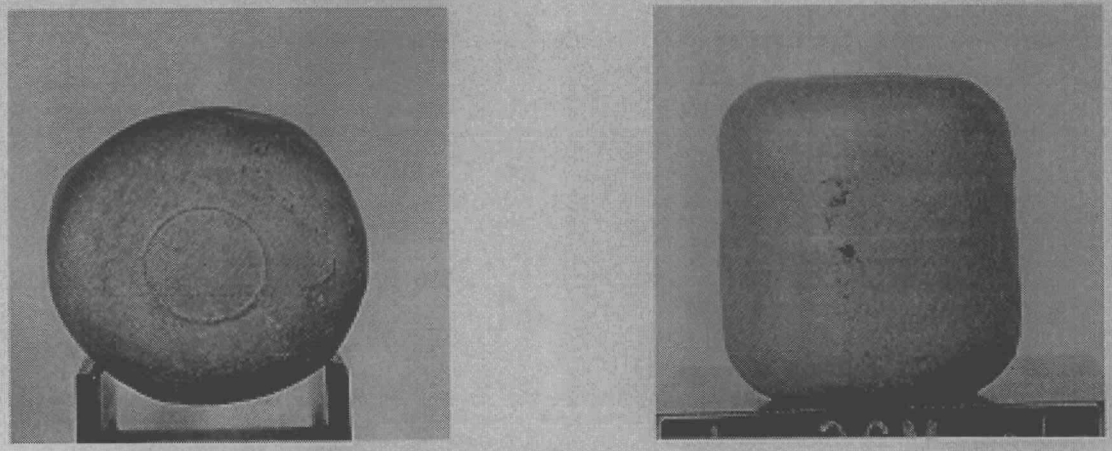

(b)

Fig. 57. CST-3 fueled clads L-12 (A GIS, blind end) and L-14 (A GIS, open end), vent end and side views. (a) Fueled clad L-12 and (b) fueled clad L-14.

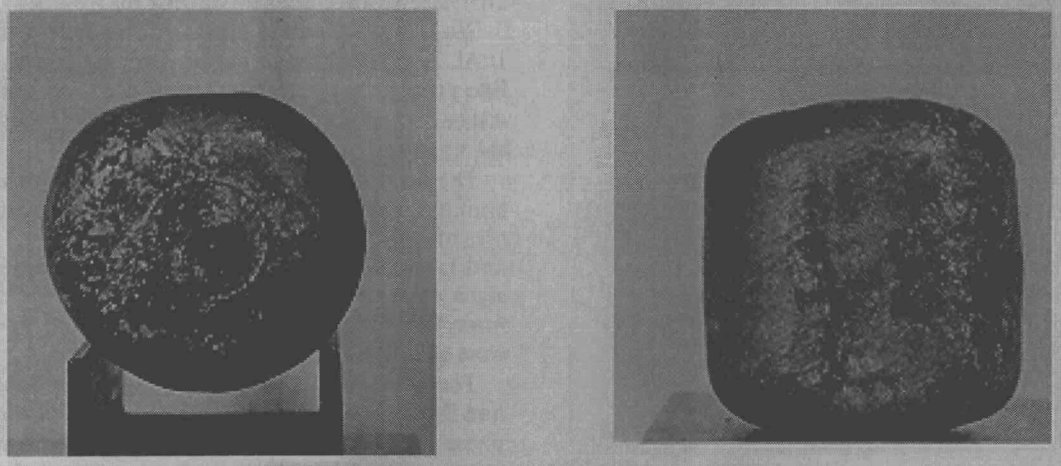

(a)

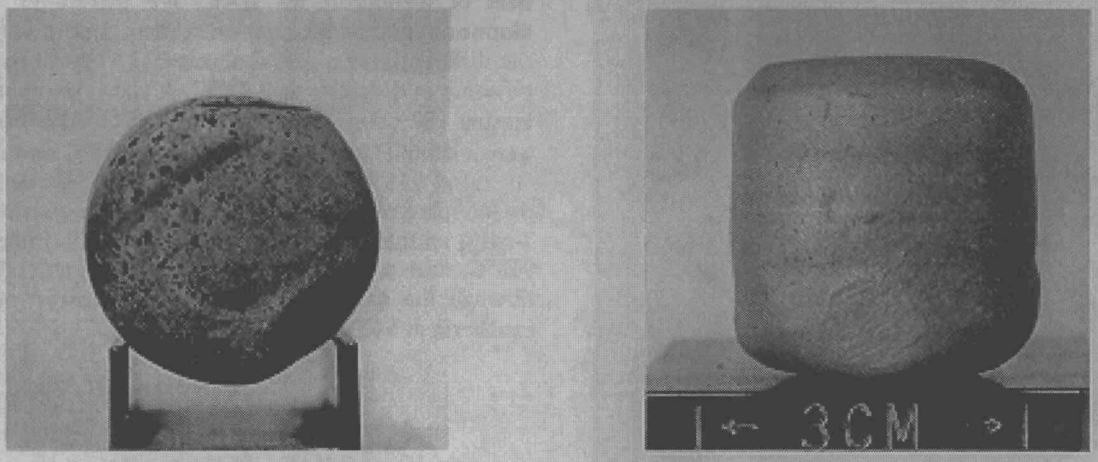

(b)

Fig. 58. CST-3 fueled clads L-16 (C GIS, blind end) and L-19 (C GIS, open end), vent end and side views. (a) Fueled clad L-16 and (b) fueled clad L-19.

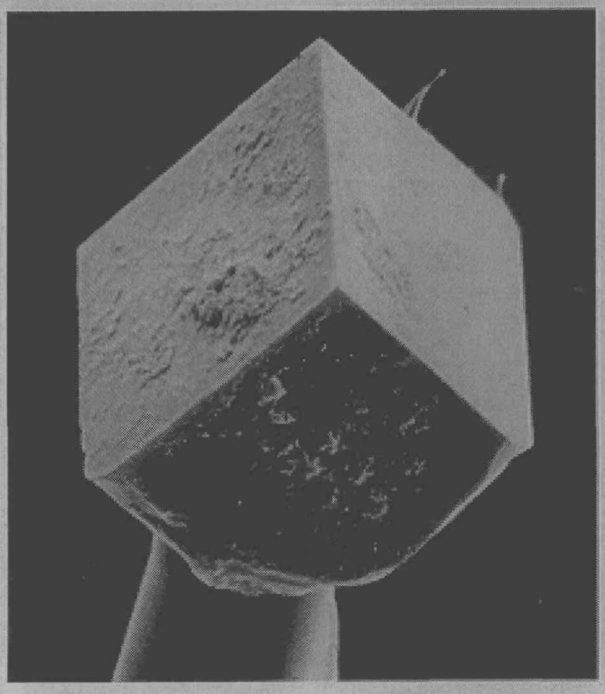

Fig. 59. Ir/Th single crystal. SEM micrograph; 250X.

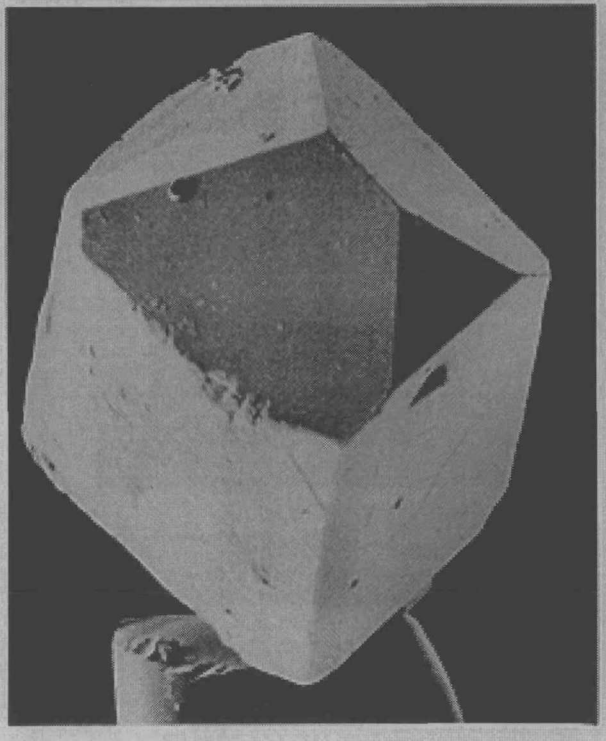

Fig. 60. Ir/P single crystal. SEM micrograph; 350X.

one specimen was annealed at 400°C for 9 weeks and the other was annealed at 800°C for 2 weeks. After the heat treatments, both specimens were resubmitted for XRD analysis; we are currently waiting for results.

We also prepared an arc-melted sample of 1:2.6 at.% Ir:Al. XRD analysis of the product generated a unique line pattern that differed from the lines associated with either IrAl or $IrAl_3$. An $IrAl_{2.7}$ compound is described in the literature.

The new multichamber tungsten cell was utilized to simultaneously induction-heat four Ir:Al powder samples of varying composition (Ir:Al ratios of 1:1, 1:2, 1:3, and 1:4) to 925°C in a vacuum. All four samples showed signs of reaction with varying amounts of unreacted material. After macroscopic examination, the samples were submitted for XRD analysis.

The XRD results indicated that the 1:1 Ir:Al mixture had formed IrAl. The 1:2 Ir:Al mixture formed a two-phase product composed of IrAl and $IrAl_3$. The 1:3 Ir:Al mixture also formed a two-phase product, but in this case only one phase ($IrAl_3$) was identifiable. The fourth sample, Ir:Al ratio 1:4, formed a single phase having a unique x-ray diffraction pattern.

2. Heats of Formation. Theoretical values for the heats of formation of various Ir/Al intermetallic compounds were calculated using a technique described in the literature by Midema. The results are presented in Table XV.

We also attempted to experimentally determine the heat of formation for $IrAl_5$. We placed 11 mg of aluminum and iridium powders in a 5:1 atomic ratio in the differential thermal analyzer (DTA) and heated the powders at 10°/min to 1500°C. A sharp exotherm, releasing 187 cal/g, maximized at 655°C. Also observed were a small (13 cal/g) endotherm at 918°C and a small (10 cal/g) 918°C exotherm at 1334°C. When we heated the sample a second time, the following were recorded: a 7-cal/g endotherm at 652°C, a 5-cal/g endotherm at 918°C, and a 14-cal/g exotherm at 1291°C. Cooling through the same region at 5°/min showed only an exotherm at 642°C (7 cal/g).

TABLE XV. Calculated Heats of Formation for Ir/Al Compounds

Compound	ΔH^{kcal}/g-atom
IrAl	−16.8
$IrAl_{2.7}$	−11.1
$IrAl_3$	−10.3
$IrAl_{3.25}$	− 8.7
$IrAl_5$	− 7.0

The exotherm at 655°C on the first heating appears to be due initially to reaction between the two elements, followed perhaps by reaction between some Al/Ir compound and one of the elements. The temperature noted is approximately the same at which a 1:1 Al:Ir mixture reacted and also corresponds to the melting point (~661°C) of the aluminum powder from which the mixes were made. The small endotherm at 652°C on the second heating and the exotherm at 642°C on cooling may therefore be due to melting/solidification of excess aluminum, which could have resulted from inaccuracies in weighing. Consequently, we believe that the heat of formation of Al_5Ir is approximately 67.4 Kcal/mol.

The small endotherm at 918°C on heating suggests formation of a high-temperature phase. The fact that a corresponding exotherm was not seen on cooling is consistent with the relatively fast cooling rate (5°/min).

C. Investigation of Th/Ir/P Ternary Compounds (K. Axler)

At the present time, a Th/Ir/P crystallization experiment, which will incorporate a longer soak time at an elevated temperature, is underway.

Another preparation was made for a crystal growth experiment with thorium, iridium, and phosphorus. In this preparation, a tin flux will be used.

D. Investigation of Th/Ir/Si Ternary Compounds (K. Axler)

Silicon is present in the GPHSs as an impurity in the fuel. The role of this element in regard to the system has been discussed and several experiments were considered. In the first test, 1:1:1 at.% Th/Ir/Si was prepared by arc melting. The material formed a clean button when melted and had a homogeneous appearance. The sample was submitted for metallography, and a section will be sent for XRD analysis.

E. Computer Modeling of GPHS Thermodynamic Behavior (K. Axler and R. Sheldon)

We are beginning an effort to thermodynamically analyze the behavior of the GPHS using the SOLGASMIX program. The software was installed on an IBM-XT computer, and testing of the program was initiated. All necessary thermodynamic properties will be contained in a data base stored along with the program on a hard disk. This approach will facilitate future system analyses.

ADDITIONAL DISTRIBUTION

B. J. Rock, Dept. of Energy/OSNP, Washington, DC
G. L. Bennett, Dept. of Energy/OSNP, Washington, DC
J. J. Lombardo, Dept. of Energy/OSNP, Washington, DC
R. B. Morrow, Dept. of Energy/OSNP, Washington, DC
R. Brouns, Dept. of Energy/OSNP, Washington, DC
J. Griffo, Dept. of Energy/OSNP, Washington, DC
D. K. Stevens, Dept. of Energy/BES, Washington, DC
M. Norin, Dept. of Energy, Washington, DC
N. P. Klug, Dept. of Energy, Washington, DC
L. Smith, Dept. of Energy, Washington, DC
E. Bjoro, Dept. of Energy, Washington, DC
G. H. Ogburn, Dept. of Energy, Washington, DC
J. A. Yoder, Dept. of Energy, Washington, DC
C. Osterberg, Dept. of Energy, Washington, DC
I. Van Der Hoven, Dept. of Energy, Rockville, MD
J. V. Dorigan, Dept. of Energy, Washington, DC
W. O. Forster, Dept. of Energy, Washington, DC
R. Watters, Dept. of Energy, Washington, DC
H. B. Rosenthal, Dept. of Energy, Washington, DC
Col. Terry Hawkins, ATSD (AE), Dept. of Defense, Washington, DC
Lt. Col. Jim Greening, HQ USAF/IG, Dept. of Defense, Washington, DC
D. L. Foster, Dept. of Energy, Albuquerque, NM
J. P. Crane, Dept. of Energy, Albuquerque, NM
K. Elliot, Dept. of Energy, Albuquerque, NM
D. L. Krenz, Dept. of Energy, Albuquerque, NM
J. R. Roeder, Dept. of Energy, Albuquerque, NM
R. B. Crouch, Dept. of Energy, Albuquerque, NM
J. N. Bailey, Dept. of Energy, Albuquerque, NM
H. N. Hill, Dept. of Energy/DOA, Miamisburg, OH
L. C. Sjostrom, Dept. of Energy, Aiken, SC
S. W. Ahrends, Dept. of Energy/ORO, Oak Ridge, TN
R. J. Hart, Dept. of Energy/ORO, Oak Ridge, TN
J. Pidkowicz, Dept. of Energy, Oak Ridge, TN
W. L. Von Flue, Dept. of Energy, SFOO, Oakland, CA
T. B. Kerr, NASA, Washington, DC
F. R. Schmidt, NASA, Washington, DC
E. Gabris, NASA, Washington, DC
N. Sculze, NASA, Washington, DC
B. R. McCullar, NASA, Washington, DC
Operations Space Shuttle, NASA, Washington, DC
A. V. Diaz, NASA, Washington, DC
R. G. Ivanoff, Jet Propulsion Laboratory, Pasadena, CA
R. W. Campbell, Jet Propulsion Laboratory, Pasadena, CA
L. C. Montgomery, Jet Propulsion Laboratory, Pasadena, CA
L. T. Shaw, Jet Propulsion Laboratory, Pasadena, CA
R. J. Spehalski, Jet Propulsion Laboratory, Pasadena, CA
Dr. Agnus D. McRonald, Jet Propulsion Laboratory, Pasadena, CA
P. Jaffe, Jet Propulsion Laboratory, Pasadena, CA
AFWL/SNS, Attn: Col. J. A. Richardson, Kirtland AFB, NM
AFWL/NTYNS, Attn: Capt. D. E. Zimmerman, Kirtland AFB, NM
Lt. Col. James H. Lee, Jr., AFWL/NTYN, Kirtland AFB, NM
Capt. Michael K. Seaton, AFWL/NTYNP, Kirtland AFB, NM
Col. John Joyce, AFISC/SND, Kirtland, AFB, NM
Maj. John Rice, AFISC/SNA, Kirtland AFB, NM
P. Dick, Teledyne Energy Systems, Timonium, MD
M. Goldman, University of California, Davis, CA
C. Smith, Sandia National Laboratories, Albuquerque, NM
R. L. Hannigan, Sandia National Laboratories, Albuquerque, NM
R. Harner, Sandia National Laboratories, Albuquerque, NM
C. M. Barnes, L. B. Johnson Space Center, NASA, Houston, TX
R. H. Brown, L. B. Johnson Space Center, NASA FM, Houston, TX
R. G. Rose, L. B. Johnson Space Center, NASA FA, Houston, TX
Harold Battaglia, L. B. Johnson Space Center, NASA PF, Houston, TX
W. H. Boggs, NASA, DE-A, J. F. Kennedy Space Center, FL
Lloyd Parker, NASA, SF, J. F. Kennedy Space Center, FL
George M. Marmaro, NASA, MD-ENV, J. F. Kennedy Space Center, FL
W. A. Riehl, Marshall Space Flight Center, NASA, EH31, Marshall SFC, AL
W. C. Pitts, NASA, STPM, Ames Research Center, Moffett Field, CA
J. J. Givens, Ames Research Center, Moffett Field, CA
R. Corridan, Ames Research Center-NASA, Moffett Field, CA
Kenneth Sutton, Langley Research Center, NASA, Hampton, VA
Gerald D. Walberg, Langley Research Center, NASA, Hampton, VA
G. J. Schaefer, Jr., Lewis Research Center, NASA, LeRo-501, Cleveland, OH
R. C. Turkolu, TRW, Defense and Space Systems Group, Redondo Beach, CA
D. Eaton, European Space Research and Technology Centre, Zwarteweg 62, Njordwijk, The Netherlands
Dr. Ralph R. Fullwood, Science Applications, Inc., Palo Alto, CA
D. Glenn, The Aerospace Corporation, Los Angeles, CA
Dr. William Ailor, The Aerospace Corporation, Los Angeles, CA
T. Carter, Nuclear Regulatory Commission, Washington, DC
C. R. Chappell, Nuclear Regulatory Commission, Washington, DC
D. E. Janes, U. S. Environmental Protection Agency, Washington, DC
D. Eagan, Office of Radiation Programs, Washington, DC
James Boland, Argonne National Laboratory-West, Idaho Falls, ID
N. Elsner, General Atomics, San Diego, CA
R. F. Abbey, Naval Research Laboratory, Washington, DC
Charles Salisbury, Naval Ocean Systems Center, San Diego, CA
Dr. Herbert Weiss, Naval Ocean Systems Center, San Diego, CA
R. Cuddihy, IIT Research Institute, Chicago, IL
J. F. Park, Pacific Northwest Laboratory, Richland, WA
Thomas M. Beasley, Oregon State University, Newport, OR
Jackson O. Blanton, Skidaway Inst. of Oceanography, Savannah, GA
Martha Scott, Texas A&M University, College Station, TX
H. James Simpson, Columbia University, Palisades, NY
S. S. Hecker, Los Alamos National Laboratory, Los Alamos, NM
R. N. R. Mulford, Los Alamos National Laboratory, Los Alamos, NM
J. Birely, Los Alamos National Laboratory, Los Alamos, NM
S. E. Bronisz, Los Alamos National Laboratory, Los Alamos, NM
W. Stark, Los Alamos National Laboratory, Los Alamos, NM
R. W. Zocher, Los Alamos National Laboratory, Los Alamos, NM
J. A. Pattillo, Los Alamos National Laboratory, Los Alamos, NM
E. M. Wewerka, Los Alamos National Laboratory, Los Alamos, NM
T. C. Wallace, Los Alamos National Laboratory, Los Alamos, NM
T. K. Keenan, Los Alamos National Laboratory, Los Alamos, NM
C. M. Seabourn, Los Alamos National Laboratory, Los Alamos, NM
P. Wagner, Los Alamos National Laboratory, Los Alamos, NM

☆ U.S. GOVERNMENT PRINTING OFFICE 1986—676-104/40003

Printed in the United States of America
Available from
National Technical Information Service
US Department of Commerce
5285 Port Royal Road
Springfield, VA 22161

Microfiche (A01)

Page Range	NTIS Price Code	Page Range	NTIS Price Code	Page Range	NTIS Price Code	Page Range	NTIS Price Code
001-025	A02	151-175	A08	301-325	A14	451-475	A20
026-050	A03	176-200	A09	326-350	A15	476-500	A21
051-075	A04	201-225	A10	351-375	A16	501-525	A22
076-100	A05	226-250	A11	376-400	A17	526-550	A23
101-125	A06	251-275	A12	401-425	A18	551-575	A24
126-150	A07	276-300	A13	426-450	A19	576-600	A25
						601 up*	A99

*Contact NTIS for a price quote.